

Point processes with event time uncertainty

Xiuyuan Cheng¹, Tingnan Gong², and Yao Xie^{2,*}

¹Department of Mathematics, Duke University

²H. Milton Stewart School of Industrial and Systems Engineering, Georgia Institute of Technology

Abstract

Point processes are widely used statistical models for continuous-time discrete event data, such as medical records, crime reports, and social network interactions, to capture the influence of historical events on future occurrences. In many applications, however, event times are not observed exactly, motivating the need to incorporate time uncertainty into point process modeling. In this work, we introduce a framework for modeling time-uncertain self-exciting point processes, known as Hawkes processes, possibly defined over a network. We begin by formulating the model in continuous time under assumptions motivated by real-world scenarios. By imposing a time grid, we obtain a discrete-time model that facilitates inference and enables computation via first-order optimization methods such as gradient descent and variational inequality (VI). We establish a parameter recovery guarantee for VI inference with an $O(1/k)$ convergence rate using k steps. Our framework accommodates non-stationary processes by representing the influence kernel as a matrix (or tensor on a network), while also encompassing stationary processes—such as the classical Hawkes process—as a special case. Empirically, we demonstrate that the proposed approach outperforms existing baselines on both simulated and real-world datasets, including the sepsis-associated derangement prediction challenge and the Atlanta Police Crime Dataset.

1 Introduction

Point processes, particularly self-exciting point processes, commonly known as Hawkes processes (see, e.g., [12, 27]), have been widely adopted for modeling sequential discrete event data across diverse domains, including seismology [22, 24, 45], social networks [8], high-frequency finance [3], and genomics [29]. Most existing models assume exact knowledge of event timestamps. However, in many practical applications, event times are often observed with uncertainty. For example, in medical contexts such as COVID-19 case reporting or ICU monitoring for sepsis detection, the exact onset of a condition may not be observed directly. Symptoms may arise, but a confirmed diagnosis typically follows after a delay due to lab testing. Similarly, in crime reports, such as burglaries, the exact time of the incident is often unknown because the event is discovered only after the fact. This type of uncertainty in event timing introduces a key modeling challenge, as illustrated in Figure 1. While timing uncertainty is critical, the literature addressing it in point processes is limited. Early efforts, such as Ogata’s Bayesian approach [23], introduced prior distributions (e.g., uniform over a fixed window) to model uncertainty in event times. However, these priors are subjective, and these methods did not fully address the computational challenges in inference.

In this paper, we introduce a new framework for modeling point processes under time uncertainty without relying on prior distributions. We adopt a non-Bayesian approach that models the underlying

*Email: yao.xie@isye.gatech.edu. Authors listed alphabetically.

continuous-time Hawkes process directly, avoiding heuristic approximations of event times. Our formulation enables principled statistical inference and leads to efficient parameter estimation algorithms with both convergence guarantees and provable recovery accuracy. Given a sequence of uncertain event-time windows, each containing at most one event, we first derive the likelihood in a continuous-time setting using a filtration defined by the history of uncertain event-window observations. In many real-world scenarios, the uncertain event windows are naturally aligned with a regular time grid (e.g., hourly medical measurements), which motivates our use of discretized time intervals. This discretization reduces the continuous-time model to a discrete-time formulation, in which the influence kernel becomes a matrix that can be estimated. This matrix is a “quantized” version of the continuous-time kernel, with its size determined by the temporal resolution and influence horizon. The resulting model can be viewed as a Bernoulli process with a link function derived specifically to map historical observations to the event probability at each time point. This structure resembles a Generalized Linear Model (GLM) for discrete-time point processes.

We develop two inference approaches based on this model: one via maximum likelihood estimation (MLE) using gradient descent, and another inspired by solving a monotone operator variational inequality (VI), adapted from [16]. The latter improves numerical stability and efficiency. We provide theoretical guarantees, including an $O(1/k)$ algorithm convergence rate for parameter recovery.

We further extend the framework to point processes on graphs, in which events are uncertain in both time and location (modeled as nodes on a graph). We begin with a continuous-time formulation and apply a similar discretization to obtain a discrete-time model. In this setting, the influence kernel becomes a tensor, indexed by both time and graph nodes, along with a baseline intensity vector over the nodes. Estimation proceeds similarly using our proposed algorithms.

Empirically, we validate the approach on synthetic data, demonstrating convergence and recovery accuracy, as well as the accuracy of our model in predicting event probabilities in future intervals under both time-only and on-network settings. To evaluate real-world utility, we apply our model to two datasets: (1) the Sepsis-Associated Derangements (SADs) dataset [28] and (2) Atlanta crime data. Both can be viewed as point processes over networks, where nodes represent medical variables or geographical regions. Our model reveals interpretable dynamic influence structures and achieves better predictive performance compared to baselines such as classical GLMs and Hawkes processes.

Notably, classical Hawkes models impose strong assumptions on the influence kernel, often fixing it to a parametric form, such as exponential decay. However, real-world influence structures can be significantly more complex. Here, we overcome this challenge by learning the influence kernel from discrete-time observations with time uncertainty, without assuming a specific parametric form. In addition, our formulation accommodates both non-stationary processes, in which the influence kernel is time-varying and represented as a matrix (or tensor in the network setting), and stationary processes, in which the kernel is time-invariant and reduces to a vector. All theoretical results and inference procedures naturally extend to the stationary case.

In summary, our contributions are:

- **Modeling:** We introduce a principled continuous-time point process model with time uncertainty, extendable to networked event data. After assuming that the event uncertainty windows are aligned with a temporal grid, the model yields a discrete-time formulation that is interpretable as a GLM with non-standard link functions.
- **Inference:** We propose efficient parameter-estimation algorithms based on solving the maximum-likelihood problem via gradient descent, as well as a new approach based on solving a variational inequality with monotone operators. We provide theoretical guarantees for the estimation algorithms, including an $O(1/k)$ convergence rate for parameter recovery.

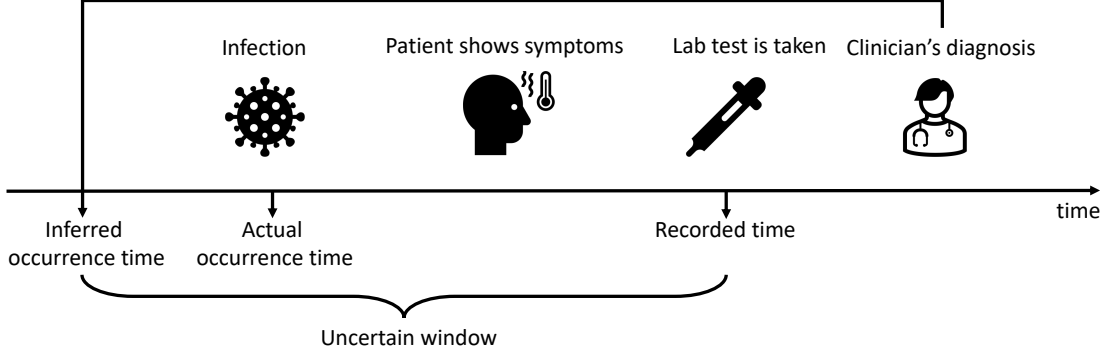


Figure 1: Illustration of a real-world medical application scenario leading to discrete event data with time uncertainty.

- **Generality:** Our framework handles both non-stationary and stationary influence kernels. All theoretical results apply to both settings.
- **Empirical validation:** We demonstrate the effectiveness of our model against baselines on both synthetic and real-world data, including the sepsis prediction dataset and the crime dataset.

Notations. The notations used in this work are standard. For a vector $x \in \mathbb{R}^n$, we use both bracket $x(u)$ or subscript x_u to denote the u -th entry of the vector. When to emphasize that x is a vector, we use the boldface symbol \mathbf{x} ; \otimes means vector outer-product, i.e., for $u, v \in \mathbb{R}^n$, $u \otimes v$ is an n -by- n matrix. $a \vee b := \max\{a, b\}$, and $a \wedge b := \min\{a, b\}$. $\mathbb{R}_+ = (0, \infty)$ denotes the set of strictly positive real numbers.

1.1 Related works

Hawkes process. The Hawkes process, originally studied in [12], is a self-exciting continuous-time point process model, which can capture the excitation effects among events. The Hawkes process [11–13] with a parametric kernel function has given rise to a body of literature for modeling the complex dynamics of heterogeneous time-event data, for example, earthquake occurrences [19, 22]. Due to its good interpretability and well-studied estimation procedures, many applied works are keen on using parametric kernels, including exponential kernels [8, 9, 38, 43] or power-law kernels [41, 42]. However, the expressiveness of the Hawkes process appears insufficient when the data are temporally non-stationary in their distribution or are not self-exciting. This is due not only to the parametric structure of the kernel in the Hawkes process, but also to the limited number of trainable parameters. Later, non-parametric Hawkes models [10], including neural Hawkes models [25], were developed to accommodate the increasing complexity of real-world applications.

Point processes beyond Hawkes. For events recorded at certain times, more expressive models have been developed in two directions. One is to model the intensity function, namely the rate of arrivals of events. Hansen et al. [10] aim to find the best linear approximation of the intensity function given a fixed dictionary. Mei and Eisner [21] model the intensity function through a continuous-time Long Short-Term Memory neural network. As indicated by [6], modeling intensity functions may lead to overfitting when the underlying dynamics are relatively simple. To address this issue, an alternative is to model the kernel function. To learn the kernel function, Zhuang et al. [46] proposed a space-time branching process model (the Epidemic Type Aftershock Sequences model) with a parametric kernel that depends on the magnitudes of ancestors, time lags from offspring to current

events, and event locations. Lewis and Mohler [17] proposed a nonparametric EM algorithm to learn coefficients for the kernel density estimator (KDE) of the triggering function. Zhou et al. [44] improved upon [17] by expressing the triggering kernel as a linear combination of base kernels rather than relying on a single KDE kernel. Bacry et al. [2] estimated the triggering kernel shape via the empirical auto-covariance of the counting process. Among these works, few explicitly consider the non-stationarity of the data in kernel design. Another line of work includes Juditsky et al. [15], who introduced a discrete-time Bernoulli process to model multivariate event data, leading to a General Linear Model (GLM) that can be efficiently optimized by first-order methods. Later, Wei and Xie [34] applied this model to learn causal networks from time-series data. These discrete-time models can be viewed as implicitly incorporating time uncertainty through discretization, but the modeling of time uncertainty itself is not explicit. In contrast, our model of event-time uncertainty is derived from the probabilistic principles of point processes and is applicable to more general point-process data. We will show that our model also leads to a GLM structure, and we adopt optimization techniques developed in [15].

Uncertainty of observations in point processes. There have been works on uncertainty quantification for model parameters of parametric Hawkes models. Wang et al. [33] quantify uncertainty in MLE estimation for multivariate Hawkes processes. Dubey et al. [7] use Bayesian neural networks to model event uncertainty via posterior distributions over model parameters. Osama et al. [26] infer confidence intervals for the intensity functions of spatial point processes. Yang et al. [39] assess model selection uncertainty using spatial point processes with applications to wildfire occurrences. These works primarily address uncertainty in model parameters rather than in the event times themselves, which is the focus of our work.

Recent studies have explored a related problem: estimating Hawkes processes from time-interval-censored observations, in which events are recorded as counts within non-overlapping time intervals. For instance, Schneider et al. [31] developed an expectation-maximization (EM) algorithm for parameter estimation in time-censored Hawkes processes. Rizoïu et al. [30] proposed an approach that approximates the Hawkes process using a Mean Behavior Poisson Process (MBPP), which assumes independent increments to simplify model fitting. However, this approximation deviates from the underlying continuous-time stochastic model of the original Hawkes process. Our model also differs from those that consider time-interval-censored observations in [30,31] in that we assume each bin contains exactly one event, a scenario in which events are rare and can be localized to specific time intervals. This setup contrasts with [30,31], where multiple events can occur within each non-overlapping bin—a more suitable model for denser observations. While our approach currently focuses on sparse event settings, it can, in principle, be extended to accommodate multiple events per bin, which we leave for future work.

Uncertainty of observations in time series. In time series analysis, uncertainty in observed values has been studied through probabilistic models [40] or interval-valued observations [18]. For a comprehensive review of uncertain time series, see the survey by Dallachiesa et al. [5]. These models are discrete in time and focus on uncertainty in observed values, whereas our work focuses on uncertainty in event timing, with our discrete-time formulation derived from continuous-time uncertainty.

2 Background

We start by reviewing some preliminaries of the classical point process without time uncertainty; a more comprehensive review can be found in [4,27].

2.1 Continuous-time Hawkes process

Given a sequence of n event times $\{t_1, t_2, \dots, t_n\}$ on $(0, T)$,

$$0 < t_1 < t_2 < \dots < t_n < T,$$

the (conditional) *intensity function* $\lambda(t)$ is defined as the probability of having the next event in $[t, t + dt)$ given the history, where we use dt to denote the infinitesimal time. Formally,

$$\lambda(t) := \lim_{\Delta t \rightarrow 0} \frac{\mathbb{E}[\mathbb{N}([t, t + \Delta t)) \mid \mathcal{H}_t]}{\Delta t}, \quad (1)$$

where \mathcal{H}_t is the history of all events up to t , and \mathbb{N} is the counting measure of the events. Define the filtration \mathcal{F}_k to be the σ -algebra generated by observations up to the k -th event, i.e.,

$$\mathcal{F}_k := \sigma\{t_1, \dots, t_k\}. \quad (2)$$

The *survival function* $S_k(t)$ is defined as

$$S_k(t) := \Pr[t_k > t \mid \mathcal{F}_{k-1}], \quad t \geq t_{k-1}, \quad (3)$$

and by definition $S_k(t_{k-1}) = 1$ and $S_k(t) > 0$.

We define the *hazard function*, $h_k(t)$ for the k -th event, in the standard fashion

$$h_k(t) := -\frac{S'_k(t)}{S_k(t)}, \quad t > t_{k-1}, \quad (4)$$

and equivalently,

$$S_k(t) = \exp \left\{ - \int_{t_{k-1}}^t h_k(s) ds \right\}, \quad t \geq t_{k-1}.$$

Thus, by definition, this gives that for each k ,

$$\Pr[t_k \in [t, t + dt) \mid \mathcal{F}_{k-1}] = -dS_k(t) = h_k(t) \exp \left\{ - \int_{t_{k-1}}^t h_k(s) ds \right\} dt. \quad (5)$$

From the above derivation, it can be shown that the intensity function $\lambda(t)$ defined in (1) actually equals the hazard function $h_k(t)$ on the interval $(t_{k-1}, t_k]$. Evaluating (5) at $t = t_k$ and applying the argument consecutively for $k = 1, \dots, n$, we have the expression of the log-likelihood as

$$\ell := \log \Pr[t_1, \dots, t_n, t_{n+1} > T] = \sum_{k=1}^n \log \lambda(t_k) - \int_0^T \lambda(s) ds.$$

The self-exciting mechanism is captured by the parametrization of the intensity $\lambda(t)$ through the *influence kernel* function $k(t', t)$ in the form as

$$\lambda[k](t) = \mu + \sum_{i, t_i < t} k(t_i, t), \quad (6)$$

where we have assumed that $\mu > 0$ is the constant base intensity of events throughout time. It is possible to make μ time-dependent in general cases.

In the classical Hawkes process [11, 13], the influence kernel $k(t', t)$ is typically assumed to be time-invariant and takes the form of an exponential function: $k(t', t) = \alpha\beta e^{-\beta(t-t')}$ where $\alpha > 0$ and $\beta > 0$ are scalar parameters. This time-invariant kernel leads to a stationary process, meaning that its distribution is invariant under time shifts. We generalize this setting by allowing $k(t', t)$ to be a time-varying influence kernel, that is, it can depend not only on the time difference $t - t'$, but also on the absolute time t . In addition, we allow the influence kernel to take negative values to account for inhibitory effects. This general form enables modeling of how past events at time t' influence future events at time $t > t'$, where the nature of this influence may vary over time. When the influence is time-invariant, the kernel simplifies to a function of the time difference, i.e., $k(t', t) = k(t - t')$. In contrast, a time-varying kernel implies that the influence of past events varies with their occurrence time t' , even for the same lag $t - t'$. Due to the principle of temporal causality, namely, that only past events can affect future events, the influence kernel is inherently asymmetric, with $k(t', t) \neq k(t, t')$ for $t \neq t'$.

2.2 Point process on networks

Hawkes already discussed the multivariate case in [12]. In a point process on a network $\mathcal{V} = \{1, \dots, V\}$ having V nodes, we observe the event data

$$(t_1, u_1), (t_2, u_2), \dots, (t_n, u_n), \quad (7)$$

over the time horizon $[0, T]$, $0 < t_1 < \dots < t_n < T$; t_i is the occurrence time of i -th event, and $u_i \in \mathcal{V}$ denotes the location of the event on the network. We can similarly define the filtration \mathcal{F}_k of precise timing and node information of events as

$$\mathcal{F}_k := \sigma\{(t_1, u_1), \dots, (t_k, u_k)\}. \quad (8)$$

The event history \mathcal{H}_t and the counting measure \mathbb{N} contain information about both event time and location. The conditional intensity function at time t and location u is defined as

$$\lambda(t, u) := \lim_{\Delta t \rightarrow 0} \frac{\mathbb{E}[\mathbb{N}([t, t + \Delta t), u) \mid \mathcal{H}_t]}{\Delta t}, \quad t > 0, u \in \mathcal{V},$$

where \mathcal{H}_t is the history of all events up to t . The log-likelihood of n events has the expression as [27]

$$\ell = \sum_{k=1}^n \log \lambda(t_k, u_k) - \int_0^T \sum_{v \in \mathcal{V}} \lambda(s, v) ds.$$

On a network, the influence kernel function $k(t', t, u', u)$ depends on both time and location. The conditional intensity function $\lambda(t, u)$ is parameterized as

$$\lambda[k](t, u) = \mu(u) + \sum_{i, t_i < t} k(t_i, t, u_i, u), \quad (9)$$

where $\mu(u) > 0$ is the base intensity at node u . The kernel function $k(t', t, u', u)$, $t > t'$, $u, u' \in \mathcal{V}$ represents the influence, that is, the triggering or inhibiting effect of the past event at time and location (t', u') on the probability of a future event at (t, u) .

The model to be introduced in Section 5 is more expressive than those previously considered in the literature (see, e.g., [27]), including the spatial-temporal factorized model $k(t', t, u', u) = k_1(t', t)k_2(u', u)$. As a result, our model can represent more complex spatial-temporal influence patterns of point processes on graphs.

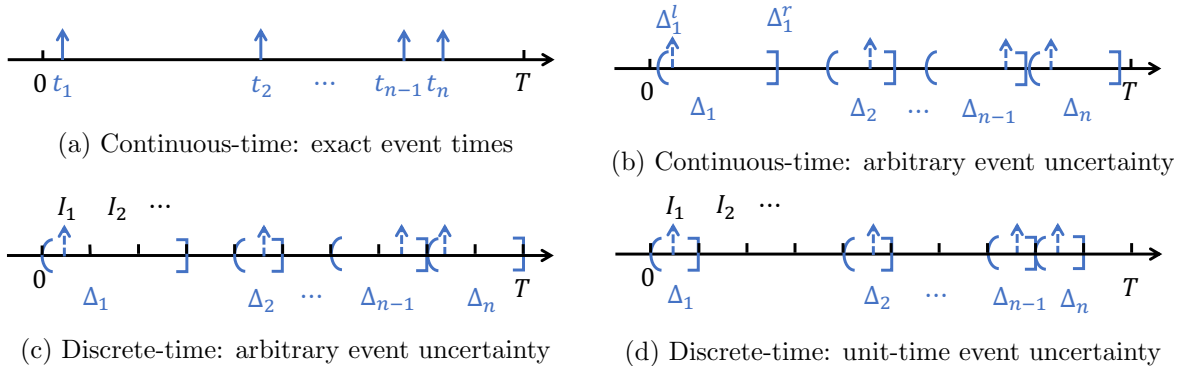


Figure 2: Illustration of the model: (a) Event times without uncertainty in the standard point process model. (b) Continuous-time model with arbitrary-length event window, see Section 3.1. (c) Discrete-time model with arbitrary-sized event uncertainty, see Section 3.2. (d) Discrete-time model with unit-sized event uncertainty, see Section 3.3.

3 Events with time uncertainty

In this section, we establish a time-uncertainty model using only event-time data, treating it as a one-dimensional point process. We first detail how to express the likelihood of a sequence of events subject to time uncertainty under a continuous-time point process model governed by a general influence kernel, and then explore a specific scenario in which the uncertainty windows align with a uniform grid on $[0, T]$. Furthermore, if the uncertainty window spans a single unit of time, the model is equivalent to a Bernoulli process with a specific link function that maps past observations to the current observation. This model will be extended to encompass network events, accounting for both time and location, in Section 5. All proofs are given in Appendix A.

3.1 Continuous-time model with arbitrary-length event window

Uncertainty window. The classical Hawkes model assumes that we observe events exactly when they occur; however, in practice, we often do not know the exact time of events. Instead, we may know when the i -th event happens up to certain *uncertainty window* Δ_i , namely,

$$t_i \in \Delta_i := (\Delta_i^l, \Delta_i^r], \quad i = 1, 2, \dots, \quad (10)$$

where $\Delta_i^l < \Delta_i^r$ are the endpoints of the interval for each event. In other words, we do not know exactly when the event happens, but we only know that it happens within the interval.

We also make the following assumption that each interval only contains one event, and the intervals do not overlap. In other words, the observation has enough time resolution to identify an individual event up to its time uncertainty.

Assumption 1 (Non-overlapping windows). (A1) *The consecutive intervals Δ_i do not overlap, i.e., $\Delta_{i-1}^r \leq \Delta_i^l$ for all i .*

We would like to remark that the extension to allow multiple events in one uncertainty window may lead to a Poisson process, which can be handled by other mathematical tools and is not the focus of this work. The time uncertainty window is illustrated in Figure 2b.

Likelihood model. We are ready to derive the likelihood of the observation

$$\mathcal{L} := \Pr[t_1 \in \Delta_1, \dots, t_n \in \Delta_n, t_{n+1} > T], \quad (11)$$

which will enable model estimation. Our derivation will be based on first principles, and we will define the survival and hazard functions in the new setting in which the history contains time uncertainty. Specifically, instead of using the filtration \mathcal{F}_k as in (2) by precise timing information, we define the filtration to be generated by historical events with time uncertainty, i.e.,

$$\tilde{\mathcal{F}}_k := \sigma\{t_i \in \Delta_i, i = 1, \dots, k\}. \quad (12)$$

For notation brevity, below we use Δ_i to stand for the probability event of $t_i \in \Delta_i$ when there is no confusion. The survival function $S_k(t)$ is defined similarly as in the classical case in Section 2.1, c.f. (3), but conditioning on the uncertain history, that is

$$S_k(t) := \Pr[t_k > t | \tilde{\mathcal{F}}_{k-1}], \quad t \geq \Delta_{k-1}^r. \quad (13)$$

Because t_k must happen after Δ_{k-1}^r by Assumption (A1), we have $S_k(\Delta_{k-1}^r) = 1$. The hazard function h_k is defined from S_k , same as before, c.f. (4),

$$h_k(t) := -\frac{S_k'(t)}{S_k(t)}, \quad t > \Delta_{k-1}^r, \quad (14)$$

and note that the time is from $t > \Delta_{k-1}^r$. As a result, $S_k(t)$ can be represented by integrating h_k as

$$S_k(t) = \exp \left\{ -\int_{\Delta_{k-1}^r}^t h_k(s) ds \right\}, \quad t \geq \Delta_{k-1}^r. \quad (15)$$

We further define the intensity function $\lambda(t)$ by *piecing together* the hazard function h_k from each interval as

$$\lambda(t) := h_k(t), \quad t \in (\Delta_{k-1}^r, \Delta_k^r], \quad k = 1, 2, \dots, \quad (16)$$

and for $k = n + 1$ it will from the interval $(\Delta_n^r, T]$; note that in this way, $\lambda(t)$ is defined everywhere on the time line.

Lemma 3.1. *The log-likelihood of \mathcal{L} as in (11) has the expression*

$$\ell := \log \mathcal{L} = \sum_{k=1}^n \log \left(\exp \left\{ \int_{\Delta_k^l}^{\Delta_k^r} \lambda(s) ds \right\} - 1 \right) - \int_0^T \lambda(s) ds. \quad (17)$$

Influence kernel. In the classical Hawkes model, the intensity function $\lambda(t)$ is further parametrized by the influence kernel function $k(t', t)$, see (6). Here, we also parametrize the intensity function (16) by a linear superposition of continuous time kernel $k(t', t)$, and we adopt the following expression to incorporate time uncertainty

$$\lambda[k](t) = \mu + \sum_{i, \Delta_i^r < t} \frac{1}{|\Delta_i|} \int_{\Delta_i^l}^{\Delta_i^r} k(t', t) dt'. \quad (18)$$

The notation has emphasized the dependence of $\lambda(t)$ on the continuous time kernel function k .

Remark 3.1 (Consistency of conditional intensity function definition). We choose the form of the conditional intensity function in (18) because it is consistent with the earlier Hawkes conditional intensity model specified in (6). Specifically, if the uncertainty window Δ_i shrinks to a single point t_k , i.e., $|\Delta_i| \rightarrow 0$ for all i , then, by that $t_i \in (\Delta_i^l, \Delta_i^r]$ according to (10) (and assuming the continuity of the function k), the expression (18) is reduced to (6). In this limit, the time-uncertain model for the conditional intensity function $\lambda(t)$ recovers the classic “time-certain” Hawkes model.

Remark 3.2 (Time-invariant kernel). In (18), we have assumed the most general form of kernel $k(t', t)$, which is allowed to be non-stationary. The time-invariant kernel is a special case when $k(t', t) = \psi(t - t')$ for some function ψ . Later in Section 4, we will first present the general case of a time-varying kernel (corresponding to the recovery of a matrix), and then discuss the special case of the time-invariant kernel (corresponding to the recovery of a vector) in Section 4.4.

3.2 Discrete time model: Arbitrary event uncertainty

In many applications, the observed uncertainty windows are some regular time intervals, e.g., a window having a length of one or more hours that starts at integer hours. For example, in the PhysioNet challenge data for sepsis prediction [28], event (patient test results) records are recorded hourly. We show that under this setting, the continuous-time uncertainty model above can be simplified into a special case of a discrete-time model, where the uncertainty is up to a certain time unit.

Time grid. We evenly divide the time horizon $(0, T)$ into N intervals, each having length h ,

$$h := T/N, \quad I_j := ((j-1)h, jh], \quad j \in [N] := \{1, \dots, N\}. \quad (19)$$

In the discrete-time models, we use h to stand for the size of the time grid, not to confuse the notation with the hazard function h_k , which was denoted by $\lambda(t)$ from (16) on.

To proceed, we assume that the event time uncertainty intervals Δ_i are “aligned” with the discrete-time grids, as illustrated in Figure 2c. We index the N intervals by the set $[N] := \{1, \dots, N\}$.

Assumption 2 (Alignment to time grid). (A2) *The uncertain event time window Δ_i can only have the end points Δ_i^l and Δ_i^r taking value on the evenly spaced discrete time grid points $\{jh : j \in [N]\}$.*

Under (A2), the event-time window Δ_i for each event i occupies some consecutive intervals of I_j . When Δ_k occupies from the l -th interval till the r -th interval, we denote the index l as t_k^l , the index r as t_k^r , that is,

$$\Delta_k = \cup_{t_k^l \leq j \leq t_k^r} I_j, \quad t_k^l, t_k^r \in [N], \quad t_k^l \leq t_k^r, \quad t_k^r < t_{k+1}^l. \quad (20)$$

The last inequality $t_k^r < t_{k+1}^l$ is by that the uncertainty windows Δ_k do not overlap as assumed in (A1). The assumption (A2) provides a discrete-time formulation that will allow us to simplify the model (17) and (18) by writing everything in discrete time indexed by $j \in [N]$.

Likelihood and influence model. Under (A2), the log-likelihood of the windowed observations (17) only depends on the N quantities which are the integral of $\lambda(t)$ on the subintervals I_j . To be specific, we define

$$\Lambda_j := \frac{1}{h} \int_{I_j} \lambda(s) ds, \quad j \in [N], \quad (21)$$

which can be interpreted as the “average intensity” over a discrete time interval I_j . With the definition of Λ_j , (17) is reduced to

$$\ell = \sum_{k=1}^n \log \left(e^{h \sum_{j'=t_k^l}^{t_k^r} \Lambda_{j'}} - 1 \right) - h \sum_{j=1}^N \Lambda_j. \quad (22)$$

Next, we derive the representation of intensity Λ_j by the influence kernel. Define the matrix

$$K_{i,j} := \frac{1}{h^2} \int_{I_i} \int_{I_j} k(t', t) dt' dt, \quad i < j, \quad i, j \in [N], \quad (23)$$

which can be interpreted as the ‘‘average influence’’ casted on the interval I_j from an earlier interval I_i . We will show that only the $i < j$ entry of $K_{i,j}$ is used. We call K the *influence kernel matrix*, which can be viewed as a quantization of the kernel function $k(t', t)$.

The following lemma provides the representation of Λ_j by the kernel matrix $K_{i,j}$.

Lemma 3.2. *Under Assumption (A2), for $j \in [N]$,*

$$\Lambda_j[K] = \mu + \sum_{\{k, t_k^r < j\}} \frac{1}{t_k^r - t_k^l + 1} \sum_{i=t_k^l}^{t_k^r} K_{i,j}. \quad (24)$$

In the notation, we have emphasized the dependence of Λ_j on the kernel matrix K . The lemma shows that the dependence of the discrete-time intensity function Λ_j from the influence kernel function $k(t', t)$ is all encoded into the matrix $K_{i,j}$.

The equations (22) and (24) provide a discrete-time model which only involves discrete-time objects Λ_j and $K_{i,j}$. This will facilitate computation, as we can thus reduce the functional optimization problem with respect to $k(t', t)$ to a matrix-valued optimization problem with respect to $K_{i,j}$.

3.3 Discrete time model: Unit-time event uncertainty

The discrete-time formulation in Section 3.2 has a simple and important special case, which we call ‘‘unit uncertainty,’’ as follows.

Assumption 3 (Unit-time uncertainty). (A3) *The uncertainty window Δ_i falls on exact one of the N intervals, i.e., $\Delta_i = I_{j(i)}$ for some $j(i) \in [N]$. In other words, $t_i^l = t_i^r = j(i)$.*

Likelihood and influence model. Under Assumption (A3), the discrete-time model (22) and (24) is further simplified to

$$\ell = \sum_{k=1}^n \log \left(e^{h\Lambda_{j(k)}} - 1 \right) - h \sum_{j=1}^N \Lambda_j, \quad \Lambda_j = \mu + \sum_{\{k: j(k) < j\}} K_{j(k),j}. \quad (25)$$

Like before, $\Lambda_j = \Lambda_j[K]$ which depends on the kernel matrix K .

Meanwhile, when the baseline intensity μ is unknown, in principle it can also be inferred from data. Thus, one can treat the scalar μ as an estimable parameter. We write the parameters $\{\mu, K\}$ together as θ , and write Λ_j as $\Lambda_j(\theta)$ to emphasize the dependence on the parametrization. In this work, our inference algorithms and experiments will focus on the unit-time uncertainty case under (A3).

In the rest of this subsection, we first show that the model (25) has an equivalent formulation in the form of a Bernoulli process, which will give a close connection to the general linear model for discrete-time point process [15] and also facilitate notations in future sections. In addition, we show that, once the parameters are estimated, our discrete-time model allows us to predict the event chance on a future interval.

Bernoulli process formulation. Under the unit-uncertainty setting (A3), our discrete-time model has an equivalent form as a Bernoulli process with an autoregressive structure and a particular link function. Below, we will use i, j , and also $t \in [N]$ to denote the time-grid index, not to be confused with the former continuous time t .

Specifically, each trajectory of the event time uncertainty window data can be written as a binary sequence $y = (y_1, \dots, y_N)$, where $y_t = 1$ if $I_t = I_{j(k)}$ for some k -th event (i.e., there is an event happening inside I_t), and $y_t = 0$ otherwise. Using the notation of y_j , (25) can be equivalently written as

$$\ell = \sum_{j=1}^N \left(-(1 - y_j)h\Lambda_j + y_j \log(1 - e^{-h\Lambda_j}) \right), \quad \Lambda_j(\theta) = \mu + \sum_{i < j} y_i K_{i,j}. \quad (26)$$

Furthermore, the following lemma characterizes the conditional expectation of y_t given the time-uncertain history. In this lemma, Λ_t refers to the true intensity Λ_t^* , namely induced by the true parameter under which the sequence $\{y_t\}_t$ is generated. The lemma provides a general linear model to predict y_t using Λ_t . We note that the link function ϕ here takes a particular form under the framework of [15], which considers a discrete-time autoregressive Bernoulli process; however, with a standard logistic link function.

Lemma 3.3. *Under the unit-uncertainty setting Assumption 3(A3) and using the formulation of the Bernoulli process y_t , for any $t \in [N]$, $\Lambda_t \in \sigma\{y_i, i \leq t-1\}$ and*

$$\mathbb{E}[y_t | y_i, i \leq t-1] = \phi(h\Lambda_t), \quad \phi(x) := 1 - e^{-x}. \quad (27)$$

The function ϕ is monotonically increasing on \mathbb{R} . The relationship (27) will be used in deriving the estimation algorithm.

Prediction on future interval. Once the parameters θ are learned from data, we can compute Λ_j based on (25) and equivalently (26). This enables us to predict the likelihood of an event occurring during a future interval. To derive the expression, we take a step back to recall the notations of the continuous-time setting in Section 3.1. Given n historical events with uncertainty, by the definition of S_k in (13), the chance of having the next event on a given interval $(l, r]$, $r > l \geq \Delta_n^r$, can be written as

$$\Pr[t_{n+1} \in (l, r] | \tilde{\mathcal{F}}_n] = S_{n+1}(l) - S_{n+1}(r). \quad (28)$$

Under the discrete-time model and using the notation in Section 3.2, suppose l and r are endpoints of the time grid that is,

$$l = j_l h, \quad r = j_r h, \quad j_r > j_l \geq t_n^r.$$

By (28), (15) and the definition of Λ_j in (21), we have

$$\Pr[t_{n+1} \in (j_l h, j_r h] | \tilde{\mathcal{F}}_n] = e^{-h \sum_{j'=t_n^r+1}^{j_l} \Lambda_{j'}} \left(1 - e^{-h \sum_{j'=j_l+1}^{j_r} \Lambda_{j'}} \right). \quad (29)$$

For the probability of having no event happening till time $l = j_l h$, we have

$$\Pr[t_{n+1} > j_l h | \tilde{\mathcal{F}}_n] = e^{-h \sum_{j'=t_n^r+1}^{j_l} \Lambda_{j'}}. \quad (30)$$

In particular, under unit-time uncertainty (A3), $\Delta_n = I_{j(n)}$ and $t_n^r = j(n)$. One can compute (29) and (30) with $t_n^r = j(n)$ in the expressions.

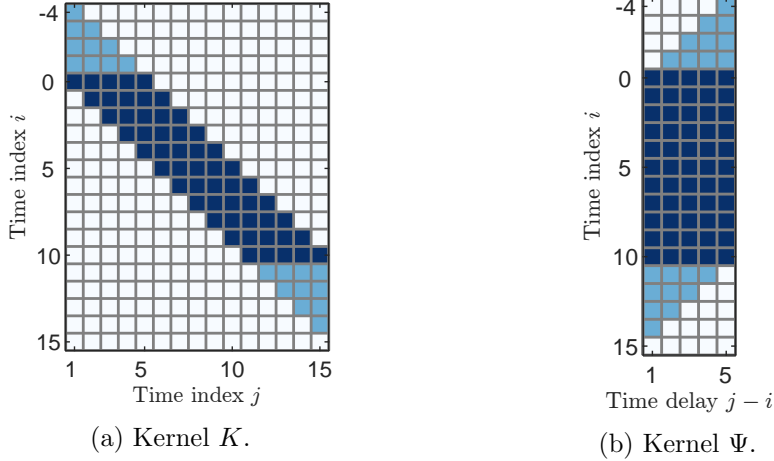


Figure 3: Kernel matrix K in (23) and the reparameterized form Ψ in (32). We set $N' = 5$ and $N = 15$. The blue (including light and dark blue) elements represent $j > i$, the entries of the kernel matrix that are estimable in θ_K , see (31); The white elements are non-causal (i.e., $j \leq i$) and thus are excluded from θ_K . We apply the low-rank constraint to the submatrix formed by the dark blue entries in Ψ .

4 Estimation of influence kernel

Given an observed sequence of event data with time uncertainty, our goal is to estimate the influence kernel from data up to the time uncertainty. The derivations in Section 3 provide a discrete-time model, where the parameters are the influence kernel matrix $\{K_{i,j}\}$ (and the scalar base intensity μ). In this section, we develop estimation approaches to recover the kernel matrix from data, focusing on unit uncertainty setting under Assumption 3(A3).

4.1 Kernel matrix and log-likelihood

Recall that θ denotes the parameters in the model, which consists of entries in the influence kernel matrix K and μ . In the model (25) and equivalently (26), only $K_{i,j}$ for $j > i$ are contributing to the likelihood. Thus, only $K_{i,j}$ for $j > i$ are included into θ . We further assume that the influence has a finite memory length, that is,

$$k(t', t) = 0, \quad \text{if } t - t' > \tau_{\max}.$$

Without loss of generality, assume that $\tau_{\max} = N'h$ for some integer N' . By definition (23), we have

$$K_{i,j} = 0, \quad \text{if } j - i > N'.$$

Thus, we only include $K_{i,j}$ for $i < j \leq i + N'$ into θ , as illustrated in Figure 3a.

The parameters are then

$$\theta = \{\mu\} \cup \{K_{i,j}, 0 < j - i \leq N', -N' < i \leq N, 0 < j \leq N\} =: \{\mu\} \cup \theta_K, \quad (31)$$

where θ_K has NN' estimable entries and thus is in the vector space of $\mathbb{R}^{NN'}$. Here, for convenience, we have assumed negative time grids indexed from $-N' + 1$ to 0 with possible observed event data (that is, the Bernoulli process model in Section 3.3 starts at $-N' + 1$ instead of 1). These historical data are used to compute Λ_j for $j > 0$, while the likelihood is computed on $1 \leq j \leq N$. The vector

θ_K can be re-arranged into an array indexed by $-N' < i \leq N$ and $0 < j - i \leq N'$, which we call the kernel matrix Ψ ,

$$\Psi_{i,l} = K_{i,i+l}, \quad l = 1, \dots, N', \quad (32)$$

and Ψ is of size $(N + N') \times N'$, see Figure 3b. In many cases, it is reasonable to assume that the rearranged kernel matrix Ψ is low-rank, possibly due to the similar influence pattern over time, see more in Section 4.4.

Using the notations above, our likelihood model (26) can be written as

$$\ell(\theta) = \sum_{t=1}^N \left(-(1 - y_t)h\Lambda_t(\theta) + y_t \log(1 - e^{-h\Lambda_t(\theta)}) \right), \quad \Lambda_t(\theta) = \mu + \langle \eta_t, \theta_K \rangle,$$

and $\eta_t \in \mathbb{R}^{NN'}$ is a vector consisting of binary-valued entries determined by the process y_t such that

$$\langle \eta_t, \theta_K \rangle = \sum_{i=t-N'}^{t-1} y_i K_{i,t}. \quad (33)$$

In practice, we usually estimate the model parameters from multiple trajectories. Given M independent (training) trajectories $\{y_t^{(m)}\}_{m=1}^M$, the log-likelihood is summed over the M trajectories. The trajectories may potentially differ in length, but the likelihood model remains well-defined. For simplicity, we assume the M trajectories are of the same length N , and the trajectories $y^{(m)}$ are i.i.d. across m . We introduce the superscript (m) to stand for the m -th trajectory and apply to the notations y_t , η_t , Λ_t and log-likelihood ℓ . We denote the (averaged) summed log-likelihood as $L(\theta)$,

$$L(\theta) = \frac{1}{M} \sum_{m=1}^M \ell^{(m)}(\theta), \quad (34)$$

$$\ell^{(m)}(\theta) = \sum_{t=1}^N \left(-(1 - y_t^{(m)})h\Lambda_t^{(m)}(\theta) + y_t^{(m)} \log(1 - e^{-h\Lambda_t^{(m)}(\theta)}) \right), \quad (35)$$

$$\Lambda_t^{(m)}(\theta) = \mu + \langle \eta_t^{(m)}, \theta_K \rangle. \quad (36)$$

Given the likelihood model, it is natural to estimate the parameters using MLE by, e.g., Gradient Descent (GD). We will see that the MLE problem is (strongly) convex under certain technical conditions, which is proved in expectation and should hold when there are enough trajectories. However, it is known that gradient descent algorithms for estimating GLMs converge slowly, particularly near the true parameters [14]. Thus, we also consider an alternative approach to estimate model parameters using Variational Inequality (VI) optimization [16]. We obtain a parameter recovery guarantee for VI (in expectation) under a stochastic optimization setting that resembles the guarantee of stochastic first-order optimization for convex problems. All the proofs are postponed to Appendix B.

4.2 Gradient Descent (GD) for MLE

Given the likelihood model (34)(35)(36), the MLE solves for parameter θ by maximizing $L(\theta)$. Again, we assume that μ is known and focus on solving for the kernel matrix parameters $z = \theta_K \in \mathbb{R}^{NN'}$. Define $L(z) := L([\mu, z])$, the GD dynamic follows the gradient field

$$F(z) = -\partial_z L(z) = \frac{1}{M} \sum_{m=1}^M \hat{F}^{(m)}(z), \quad \hat{F}^{(m)}(z) = -\partial_z \ell^{(m)}([\mu, z]),$$

and the GD update is by $z_k = z_{k-1} - \gamma_k F(z_{k-1})$ at step size $\gamma_k > 0$. One can also implement stochastic optimization similar as in (39), replacing $\hat{G}^{(k)}$ with $\hat{F}^{(k)}$.

Direct computation gives the expression of $\hat{F}^{(m)}$ as

$$\hat{F}^{(m)}(z) = \sum_{t=1}^N \frac{h}{\phi(h\Lambda_t^{(m)}(z))} (\phi(h\Lambda_t^{(m)}(z)) - y_t^{(m)}) \eta_t^{(m)}, \quad (37)$$

as well as the Hessian of $L(z)$. The following proposition shows that the objective $-L$ is strongly convex in expectation on the domain Θ_K .

Proposition 4.1. *Under Assumption 4, $-\mathbb{E}L(z)$ is κ' -strongly convex on Θ_K , where $\kappa' := e^{-2hb}(b/B)^2 h^2 e^{-B\tau_{\max}}$.*

While Proposition 4.1 gives an in-expectation result, one may use the i.i.d. or possibly relaxed independence assumptions on trajectories $y^{(m)}$ to derive a concentration argument and show that when there are sufficiently many training trajectories, $-L$ is strongly convex and the MLE has a unique solution. Meanwhile, it is also possible to prove a recovery guarantee (in expectation) for a stochastic GD scheme similar to the VI result in Theorem 4.5. We omit these extensions.

4.3 Monotone Variational Inequality (VI) for parameter recovery

The VI approach leverages the GLM model in (27) with link function $\phi : \mathbb{R} \rightarrow \mathbb{R}$, and casts the parameter estimation problem as finding an equilibrium that corresponds to the true parameters using an iteration defined by the monotone operator [15, 16]. We conceptually consider the L^2 loss defined as $L_{\text{VI}}(\theta) = \frac{1}{M} \sum_{m=1}^M \ell_{\text{VI}}^{(m)}(\theta)$, where

$$\ell_{\text{VI}}^{(m)}(\theta) = \frac{1}{2h} \sum_{t=1}^N (\phi(h\Lambda_t^{(m)}(\theta)) - y_t^{(m)})^2.$$

Recall that $\theta = \{\mu, \theta_K\}$. For simplicity and without loss of generality, in the rest of this section, we always assume that μ is a known constant and focus on estimating the influence kernel $\theta_K \in \mathbb{R}^{NN'}$. We will explain the algorithmic details to recover μ from data in Section 6.

VI stochastic scheme. For notation convenience, we denote θ_K as $z \in \mathbb{R}^{NN'}$, and also write $\Lambda_t(z) = \Lambda_t([\mu, z])$, i.e., with $\theta = [\mu, z]$. Note that $\Lambda_t^{(m)}$ is linear in $z = \theta_K$ and $\partial_{\theta_K} \Lambda_t^{(m)}(\theta) = \eta_t^{(m)}$ by (36). Following the VI monotone operator construction for GLM [15], we have the VI monotone operator (as a vector field in the space of z and it is *not* the gradient to minimize the L^2 loss above, which is a non-convex problem) written as

$$\hat{G}(z) = \frac{1}{M} \sum_{m=1}^M \hat{G}^{(m)}(z), \quad \hat{G}^{(m)}(z) = \sum_{t=1}^N \left(\phi(h\Lambda_t^{(m)}(z)) - y_t^{(m)} \right) \eta_t^{(m)}. \quad (38)$$

We use z_k to stand for the parameter at the k -th iteration, $k = 0, 1, \dots$. The stochastic updating scheme reads

$$z_k = \text{Proj}_{\Theta_K} [z_{k-1} - \gamma_k \hat{G}^{(k)}(z_{k-1})], \quad (39)$$

where $\gamma_k > 0$ is the step size, Θ_K is a convex compact domain in $\mathbb{R}^{NN'}$ satisfying certain technical assumptions to be specified below, and Proj_{Ω} is the metric projection operator onto convex set Ω defined as

$$\text{Proj}_{\Omega}(z) := \arg \min_{u \in \Omega} \|u - z\|_2^2. \quad (40)$$

We assume that the iteration (39) starts from $z_0 \in \Theta_K$. For theoretical simplicity, we also assume there are enough trajectories to compute (39) without repeating.

Kernel recovery guarantee. We will prove the convergence of the scheme (39) such that z_k recovers the true kernel parameter z^* . The convergence bounds the 2-norm error in expectation, namely $\mathbb{E}\|z_k - z^*\|_2^2$, where the expectation \mathbb{E} is over the randomness of data observations $y_t^{(m)}$. A central property of analyzing VI optimization is the monotonicity of the VI vector field. We define

$$G(z) := \mathbb{E}\hat{G}^{(m)}(z) = \mathbb{E} \sum_{t=1}^N (\phi(h\Lambda_t(z)) - y_t) \eta_t, \quad (41)$$

and when z is the true kernel z^* we have

$$G(z^*) = 0, \quad (42)$$

as a result of Lemma 3.3 (in (41), first taking conditional expectation conditioning on $y_i, i \leq t-1$). We will see that the strong monotonicity of $G(z)$ can be induced when $\mathbb{E} \sum_{t=1}^N \eta_t \otimes \eta_t$ is strictly positive definite.

To proceed, we introduce the following assumption on the domain Θ_K of z .

Assumption 4 (Physical intensity). *There exist constants $B, b > 0$ s.t.*

(i) *The true conditional intensity Λ_t^* satisfies*

$$b \leq \Lambda_t^* \leq B, \quad \forall t = -N' + 1, \dots, N, \quad a.s. \quad (43)$$

(ii) *There exists a non-empty, compact, and convex set $\Theta_K \subset \mathbb{R}^{NN'}$ such that the true kernel parameter $z^* \in \Theta_K$, and for any $z \in \Theta_K$,*

$$b \leq \Lambda_t(z) \leq B, \quad \forall t = 1, \dots, N, \quad a.s. \quad (44)$$

To clarify the relationship of Λ_t^* and z^* , note that z^* is the true kernel matrix restricted to the NN' entries in (31). Thus $\Lambda_t^* = \Lambda_t(z^*)$ when $1 \leq t \leq N$, and Λ_t^* for $-N' < t \leq 0$ also involves entries of the true kernel outside the NN' index set.

We say that the intensity $\Lambda_t(z) > 0$ is “physical”. Assumption 4(ii) imposes that the model intensity $\Lambda_t(z)$ is upper and lower bounded by positive constants. For example, when $z = 0$, $\Lambda_t \equiv \mu$. Then, as long as $[b, B]$ contains μ , we have (44) hold at $z = 0$. Thus, one can initialize the iteration (39) from $z_0 = 0$ assuming that $0 \in \Theta_K$. On the other hand, Assumption 4(i) actually implies the following lemma:

Lemma 4.2. *Under Assumption 4(i), we have that $\mu \in [b, B]$, and any realization of the binary sequence $\{y_t, -N' < t \leq N\}$ happens w.p. > 0 . Consequently, it always holds that $b \leq \Lambda_t^* \leq B$, $\forall t = -N' + 1, \dots, N$.*

As a result, the requirement that (44) holds a.s. means that the model intensity $\Lambda_t(z)$ also needs to stay in $[b, B]$ for any realization of the history sequence $\{y_i, t - N' \leq i \leq t - 1\}$. This poses finitely many linear constraints on z as a vector.

We are ready to prove the strict positive definiteness of $\mathbb{E} \sum_{t=1}^N \eta_t \otimes \eta_t$:

Lemma 4.3. *Under Assumption 4(i),*

$$\mathbb{E} \sum_{t=1}^N \eta_t \otimes \eta_t \succeq \rho I_{NN'}, \quad \rho := (1 - e^{-hb})e^{-hB(N'-1)}.$$

Lemma 4.4 (Strong monotonicity of $G(z)$). *Under Assumption 4, $G(z)$ is κ -monotone on Θ_K , where*

$$\kappa := e^{-hb}bh^2e^{-B\tau_{\max}}. \quad (45)$$

Theorem 4.5 (Kernel recovery by VI). *Under Assumption 4, suppose $y^{(k)} = \{y_t^{(k)}\}_t$ are i.i.d. trajectories across k , and z_k is computed from (39) starting from $z_0 \in \Theta_K$, with step size*

$$\gamma_k = \frac{1}{\kappa(k+1)},$$

where κ is as in (45). Then, with $C := B(T + \tau_{\max}) \wedge (N + N')$, we have

$$\mathbb{E}\|z_k - z^*\|_2^2 \leq \frac{4C^2}{\kappa^2} \frac{1}{k+1}, \quad k = 0, 1, \dots$$

As will be shown in the proof, the i.i.d. trajectory assumption is only used to ensure that $\mathbb{E}[\hat{G}^{(k)}(z_{k-1})|y^{(m)}, m = 1, \dots, k-1] = G(z_{k-1})$ and thus can potentially be relaxed. Meanwhile, Theorem 4.5 gives an “in-expectation” parameter recovery bound, and to derive a recovery guarantee beyond the in-expectation type result, one can use the i.i.d. or possibly relaxed independence assumptions on samples to induce concentration of the error $\|z_k - z^*\|$ around its expectation. Such theoretical extensions are omitted here.

Remark 4.1 (Scaling in the continuity limit). We consider the limit when the length of the time grid interval $h \rightarrow 0$, where the kernel matrix K approaches the kernel function $k(t', t)$ and the time-uncertainty model (the unit-uncertainty setting) approaches the time-certain case. We assume that the time horizon $T = hN$ and the influence time lag $\tau_{\max} = hN'$ stay as $O(1)$ constants in the limit, and we call this the *continuity limit*. In other words, $N \sim N' \sim 1/h$. We also assume that the constants b and B in Assumption 4 are fixed positive constants. In this asymptotic, for large N (and N') and equivalently small h , $C \sim B(T + \tau_{\max})$ is $O(1)$, and $\kappa \sim h^2e^{-B\tau_{\max}}$, and thus the factor C/κ in the convergence bound in Theorem 4.5 scales as $e^{B\tau_{\max}}/h^2$, which $\sim h^{-2}$ and we kept the exponential factor in the constant.

In practice, we compute the VI using batch-based stochastic updates, and the constraint of Λ_t being physical, corresponding to the lower bound in Assumption 4(ii), is enforced by a barrier penalty. The details will be introduced in Section 6.

We give a few comments on the comparison of the GD and VI optimization dynamics: First, consider the continuity limit (Remark 4.1), since b and B are fixed $O(1)$ constants, both the (in expectation) VI monotonicity modulus κ (Lemma 4.4) and the GD convexity κ' (Proposition 4.1) scale as $h^2e^{-B\tau_{\max}}$, here we keep the $O(1)$ factor $e^{-B\tau_{\max}}$ which is exponential. In short, κ and κ' both $\sim h^2$ which are comparable. This suggests that, in theory, the in-expectation convergence behavior of the two optimization approaches is comparable; for example, the convergence rate should be the same up to a constant factor.

However, comparing the GD gradient field (37) to the VI gradient field (38), we see that $\hat{F}^{(m)}$ has an extra multiplicative factor $h/\phi(h\Lambda_t^{(m)}(z))$ for each time t . While $\phi(h\Lambda_t^{(m)}(z)) \sim h$ under Assumption 4, and thus this factor does not change the order of magnitude of the gradient field, the term $\phi(h\Lambda_t^{(m)}(z))$ on the denominator is a random variable and can introduce additional fluctuation especially when the conditional intensity at t is small. This is consistent with our empirical observation that VI dynamics are more stable than GD, see Appendix D.3.4.

4.4 Special structures in influence kernel

Time-invariant kernel. When the influence kernel $k(t', t)$ is time-invariant, see Remark 3.2, we know that the kernel matrix K has the pattern that $K_{i,j} = \Psi_{i,j-i} = \psi_{j-i}$, where $\{\psi_l, l = 1, \dots, N'\}$ is a vector of length N' . Thus, the parameters in the kernel matrix are the vector $\psi \in \mathbb{R}^{N'}$, assuming that μ is known and fixed. The likelihood model (34)(35) still holds, where the kernel parametrization of $\Lambda_t^{(m)}$ is

$$\Lambda_t^{(m)}(\psi) = \mu + \langle \xi_t^{(m)}, \psi \rangle, \quad \text{where } \langle \xi_t, \psi \rangle = \sum_{i=t-N'}^{t-1} y_i \psi_{t-i}. \quad (46)$$

The vector $\xi_t \in \mathbb{R}^{N'}$ consists of binary-valued entries determined by the history of y_t from $t - N'$ to $t - 1$. The estimation by VI and GD applies here, and the optimization is reduced to solving for the vector ψ of dimension N' instead of the kernel parameter θ_K of dimension NN' as in (31). We provide additional details on VI recovery below.

Similar to (38), the VI vector field is

$$\hat{G}_s(\psi) = \frac{1}{M} \sum_{m=1}^M \hat{G}_s^{(m)}(\psi), \quad \hat{G}_s^{(m)}(\psi) = \sum_{t=1}^N \left(\phi(h\Lambda_t^{(m)}(\psi)) - y_t^{(m)} \right) \xi_t^{(m)}, \quad (47)$$

and we use the subscript $_s$ to stand for “stationary”. Define

$$G_s(\psi) := \mathbb{E} \hat{G}_s^{(m)}(\psi) = \mathbb{E} \sum_{t=1}^N (\phi(h\Lambda_t(\psi)) - y_t) \xi_t, \quad (48)$$

and again we have $G_s(\psi^*) = 0$ where ψ^* is the true time-invariant kernel. We assume that the true conditional intensity Λ_t^* satisfies Assumption 4(i), and similar to (ii) we assume that

(ii') There exists a non-empty, compact and convex set $\Theta_\psi \subset \mathbb{R}^{N'}$ such that the true kernel parameter $\psi^* \in \Theta_\psi$, and for any $\psi \in \Theta_\psi$, $b \leq \Lambda_t(\psi) \leq B$, $\forall t = 1, \dots, N$, a.s.

Lemma 4.2 still applies. The following lemma is a counterpart of Lemma 4.4.

Lemma 4.6 (Strong monotonicity of $G_s(z)$). *Suppose the influence kernel is time-invariant, under Assumption 4(i) and the assumption (ii') on Θ_ψ as above, $G_s(\psi)$ is κ_s -monotone on Θ_ψ , where*

$$\kappa_s := e^{-hb} b T h e^{-B\tau_{\max}}.$$

Based on Lemma 4.6, one can prove a VI recovery result similar to Theorem 4.5. Specifically, let ψ_k be the sequence computed from the stochastic VI scheme; we have

$$\mathbb{E} \|\psi_k - \psi^*\|_2^2 \leq \frac{4C_s^2}{\kappa_s^2} \frac{1}{k+1}, \quad k = 0, 1, \dots,$$

where C_s is an $O(1)$ constant involving B , T and τ_{\max} and derived using a similar argument as Lemma B.1. Our asymptotic notation here refers to the continuity limit per Remark 4.1. Note that $\kappa_s \sim h e^{-B\tau_{\max}}$ while previously with time-varying kernel $\kappa \sim h^2 e^{-B\tau_{\max}}$. As a result, the factor C_s/κ_s in the convergence bound $\sim h^{-1}$, while previously in Theorem 4.5, the factor $C/\kappa \sim h^{-2}$. This improvement is essentially because with a time-invariant kernel, we have $N' \sim h^{-1}$ many parameters to recover, while with a time-varying kernel, there are $NN' \sim h^{-2}$ many parameters.

Low-rank structure. There are different possible ways to impose low-rank structures on the influence kernel, and in our discrete-time model, naturally on the kernel matrix. Recalling the representation of the kernel matrix as K and Ψ in Section 4.1 and Figure 3. We think it is natural to impose the low-rank structure on Ψ , as previously adopted in [6] for influence kernel functions. In particular, the time-invariant kernel corresponds to the case where $\Psi = \mathbf{1}_N \psi^T$ (after filling the entries outside the region of NN' entries to be recovered from data), that is, Ψ is a rank-1 matrix.

Theoretically, the kernel matrix is constructed by a grid average of the kernel function, see (23). Thus, the low rankness of the kernel matrix can be a result of the discretization of a continuous kernel function $k(t', t)$, assumed to have certain regularity with respect to the varying times t' and t . In Section 7, we experimentally study several simulated examples where the kernel matrix is induced from some continuous function k , and numerically, the matrix Ψ can be approximated by a low-rank matrix.

We need some additional tricks when applying the low-rank constraint in practice. As has been explained in Section 4.1, the NN' learnable parameters in θ_K form a parallelogram-shaped region in the matrix Ψ which is of size $(N + N') \times N'$, see Figure 3b. Thus, even the underlying Ψ has low-rankness (after filling the $(N + N') \times N'$ matrix), the inferred Ψ by optimization has no values (or zero values) outside the parallelogram region, and this interferes with the low-rankness. To overcome this issue, observe that when Ψ is rank- r , then any $m \times N'$ submatrix Ψ' of Ψ (by retrieving rows) is at most rank- r , and the rows of Ψ' are spanned by the r right singular vectors of Ψ . We choose the submatrix Ψ' to be the “middle chunk” of Ψ that has full rows inside the parallelogram region, indicated by dark blue entries in Figure 3b. In practice, we impose low rankness on Ψ' using a truncated SVD, and use the right singular vectors of Ψ' to apply a projection of the inferred full matrix Ψ , see more in Section 6.

5 Time-uncertainty point process on network

In this section, we extend the time uncertainty model to the network setting, namely when the event data also contains location information u_i for the i -th event and u_i is a node on a graph. All the proofs can be found in Appendix C.

5.1 Continuous-time formulation

Filtration and conditional intensity. We consider the event data on a network $\mathcal{V} = \{1, \dots, V\}$ where the event time t_i has uncertainty, and the event location $u_i \in \mathcal{V}$. The classical scenario with exact event time is provided in (7), as a comparison. Following the formulation in Section 3, we consider $t_i \in \Delta_i$ same as before. Again, let Δ_i also denote the event that $\{t_i \in \Delta_i\}$, the filtration is defined as

$$\tilde{\mathcal{F}}_k := \sigma\{(\Delta_i, u_i), i = 1, \dots, k\}.$$

We define the survival function $S_k(t)$ and hazard function $h_k(t)$ same as in (13) and (4), respectively, that is, $S_k(t)$ and $h_k(t)$ only addresses the time of the event regardless of the event location. We then have that (14)(15) also hold.

To be able to incorporate event location information u_i , we define $\tilde{f}_k(u|t)$ by

$$\tilde{f}_k(u|t) := \Pr[u_k = u | t_k \in [t, t + dt), \tilde{\mathcal{F}}_{k-1}], \quad (49)$$

and then, for $t > \Delta_{k-1}^r$,

$$\begin{aligned}
\Pr[t_k \in [t, t + dt), u_k = u | \tilde{\mathcal{F}}_{k-1}] &= \Pr[t_k \in [t, t + dt) | \tilde{\mathcal{F}}_{k-1}] \tilde{f}_k(u|t) \\
&= -S'_k(t) \tilde{f}_k(u|t) dt \\
&= S_k(t) h_k(t) \tilde{f}_k(u|t) dt \quad (\text{by (14)}) \\
&= S_k(t) \lambda(t, u) dt,
\end{aligned} \tag{50}$$

where we define

$$\lambda(t, u) := h_k(t) \tilde{f}_k(u|t). \tag{51}$$

By that $\tilde{f}_k(u|t)$ is a conditional distribution of $u \in \mathcal{V}$ and thus $\sum_{u \in \mathcal{V}} \tilde{f}_k(u|t) = 1$, we have

$$\sum_{u \in \mathcal{V}} \lambda(t, u) = h_k(t) =: \bar{\lambda}(t), \tag{52}$$

where we define $\bar{\lambda}(t)$ to equal $h_k(t)$ piece-wisely on $(\Delta_{k-1}^r, \Delta_k^r]$, similarly as in (16). Back to (50), by integrating dt over the interval Δ_k on both sides, we have

$$\begin{aligned}
\Pr[t_k \in \Delta_k, u_k = u | \tilde{\mathcal{F}}_{k-1}] &= \int_{\Delta_k^l}^{\Delta_k^r} S_k(t) \lambda(t, u) dt \\
&= \int_{\Delta_k^l}^{\Delta_k^r} \lambda(t, u) e^{-\int_{\Delta_{k-1}^r}^t h_k(s) ds} dt \quad (\text{by (15)})
\end{aligned} \tag{53}$$

$$= e^{-\int_{\Delta_{k-1}^r}^{\Delta_k^r} \bar{\lambda}(s) ds} \int_{\Delta_k^l}^{\Delta_k^r} \lambda(t, u) e^{\int_t^{\Delta_k^r} \bar{\lambda}(s) ds} dt. \tag{54}$$

Likelihood model. With these notions in hand, in the following lemma, we derive the expression of the likelihood

$$\mathcal{L} := \Pr[(\Delta_1, u_1), \dots, (\Delta_n, u_n), t_{n+1} > T]$$

Lemma 5.1. *Recall that $\bar{\lambda}(t) = \sum_{u \in \mathcal{V}} \lambda(t, u)$,*

$$\log \mathcal{L} = \sum_{k=1}^n \log \left(\int_{\Delta_k^l}^{\Delta_k^r} \lambda(t, u_k) e^{\int_t^{\Delta_k^r} \bar{\lambda}(s) ds} dt \right) - \int_0^T \bar{\lambda}(s) ds. \tag{55}$$

Remark 5.1 (Reduction to classical scenario without time uncertainty). We consider the limit where the length of the window Δ_i shrinks to zero, that is, $\Delta_i^l, \Delta_i^r \rightarrow t_i$ the certain event time for all i . We claim that in this case,

$$\frac{1}{|\Delta_k|} \Pr[t_k \in \Delta_k, u_k = u | \tilde{\mathcal{F}}_{k-1}] \rightarrow \lambda(t_k, u) e^{-\int_{t_{k-1}}^{t_k} \bar{\lambda}(s) ds}. \tag{56}$$

This is can be derived from (53), which gives that the l.h.s. can be written as

$$\frac{1}{|\Delta_k|} \int_{\Delta_k^l}^{\Delta_k^r} \lambda(t, u) e^{-\int_{\Delta_{k-1}^r}^t \bar{\lambda}(s) ds} dt,$$

and then using the continuity of $\lambda(t, u)$ (and $\bar{\lambda}(t)$) with respect to t . The equation (56) leads to the expression

$$\Pr[(t_k, u) | \mathcal{F}_{k-1}] = \lambda(t_k, u) e^{-\int_{t_{k-1}}^{t_k} \bar{\lambda}(s) ds},$$

where we recall that in the classical (time-certain) model, $\mathcal{F}_k := \sigma\{(t_i, u_i), i = 1, \dots, k\}$. Then, the log-likelihood of the n events can be shown to be

$$\log \mathcal{L} = \sum_{k=1}^n \log \lambda(t_k, u_k) - \int_0^T \bar{\lambda}(s) ds,$$

which recovers the classical model without time uncertainty, see e.g. Eqn (8) in [27].

Remark 5.2 (Reduction to time-only model). Consider the special case where the network \mathcal{V} only has one node u . In this case, $\bar{\lambda}(t) = \lambda(t, u)$ and define it to be $\lambda(t)$. Then, one can verify that

$$\int_{\Delta_k^l}^{\Delta_k^r} \lambda(t) e^{\int_t^{\Delta_k^r} \lambda(s) ds} dt = e^{\int_{\Delta_k^l}^{\Delta_k^r} \lambda(s) ds} - 1.$$

This equality reduces the conditional probability (54) to (A.1), and the log-likelihood (55) to (17). That is, the model is reduced to the time-only case in Section 3.1.

Influence kernel. We introduce the spatial-temporal influence kernel function $k(t', t; u', u)$ to parametrize the intensity function $\lambda(t, u)$. By incorporating the spatial dependence in (18), we have

$$\lambda[k](t, u) = \mu(u) + \sum_{i, \Delta_i^r < t} \frac{1}{|\Delta_i|} \int_{\Delta_i^l}^{\Delta_i^r} k(t', t; u_i, u) dt', \quad (57)$$

where $\mu(u) > 0$ for $u \in \mathcal{V}$ is the base intensity on the network \mathcal{V} . Based on the continuous-time model (55) and (57), we will derive a discrete-time model in the next subsection under additional assumptions.

5.2 Discrete-time model and discrete parametrization

We consider the time grid as in Section 3.2 which has N intervals I_j , $|I_j| = h = T/N$. For simplicity, we only consider the unit uncertainty setting as in Assumption 3(A3).

Time-quantized influence kernel. Suppose $\Delta_k = I_{j(k)}$, the log-likelihood (55) can be written as

$$\log \mathcal{L} = \sum_{k=1}^n \log \left(\int_{I_{j(k)}^l}^{I_{j(k)}^r} \lambda(t, u_k) e^{\int_t^{I_{j(k)}^r} \bar{\lambda}(s) ds} dt \right) - \int_0^T \bar{\lambda}(s) ds. \quad (58)$$

This, however, still cannot be expressed by the average of $\lambda(t, u)$ on $t \in I_j$ only, due to that $\lambda(t, u) e^{\int_t^{I_{j(k)}^r} \bar{\lambda}(s) ds}$ takes different value over location u and $t \in I_{j(k)}$. To reduce to a discrete problem, we introduce the following assumption on the influence kernel.

Assumption 5 (Time-quantized influence kernel on network). *For any $u', u \in \mathcal{V}$ and $1 \leq i < j \leq N$, $k(t', t; u', u)$ is constant on $(t', t) \in I_i \times I_j$, and we denote the value as $K_{i,j}(u', u)$.*

A useful consequence of the assumption is that the influence function $\lambda(t, u)$ is also quantized in time, which is proved in the following lemma.

Lemma 5.2 (Discrete-time intensity). *Under (A3) and Assumption 5, for any $u \in \mathcal{V}$, $\lambda(t, u)$ as defined in (57) is constant over $t \in I_j$. We denote the value as $\Lambda_j(u)$, and*

$$\Lambda_j(u) = \mu(u) + \sum_{\{k: j(k) < j\}} K_{j(k), j}(u_k, u). \quad (59)$$

Likelihood model and learnable parameters. According to (52), we define

$$\bar{\Lambda}_j = \sum_{u \in \mathcal{V}} \Lambda_j(u). \quad (60)$$

The following lemma derives the log-likelihood which only involves $\{\Lambda_j(u), j \in [N], u \in \mathcal{V}\}$.

Lemma 5.3 (Discrete-time likelihood on network). *Under Assumption 3(A3) and Assumption 5, the log-likelihood defined in (55) can be written as*

$$\ell := \log \mathcal{L} = \sum_{k=1}^n \log \left((e^{h\bar{\Lambda}_{j(k)}} - 1) \frac{\Lambda_{j(k)}(u_k)}{\bar{\Lambda}_{j(k)}} \right) - h \sum_{j=1}^N \bar{\Lambda}_j, \quad (61)$$

The parameters in the model are the baseline intensities $\mu(u)$ and the influence kernel $K_{i,j}(u', u)$, both of which are on the network, which determines the network conditional intensities $\Lambda_j(u)$ as in (59). Adopting the same time-grid setup in Section 4.1, we consider the extended time grid from $-N' + 1$ to N , where the max time lag for influence is $\tau_{\max} = N'h$. Denoting the learnable parameters as θ , we have

$$\theta = \{\mu(u), u \in \mathcal{V}\} \cup \{K_{i,j}(u', u), u', u \in \mathcal{V}, 0 < j - i \leq N', -N' < i \leq N, 0 < j \leq N\}. \quad (62)$$

We similarly introduce the rearranged kernel matrix Ψ , where

$$\Psi_{i,l}(u', u) = K_{i,i+l}(u', u), \quad \forall u', u \in \mathcal{V}, \quad l = 1, \dots, N'. \quad (63)$$

We will discuss the estimation of parameters from data in Section 5.4.

Prediction on future interval. Extending the argument in Section 3.3, we can predict the probability of having the next event happen during a future interval and at a location on \mathcal{V} once the parameter θ is learned from data. Specifically, recall the notations in the continuous-time setting in Section 5.1, we are given n historical events and the goal is to predict the probability of the $(n+1)$ -th event happening on the interval $(l, r]$, $r > l \geq \Delta_n^r$. Using the discrete-time model under (A3), $\Delta_n = I_{j(n)}$, and again suppose l and r are endpoints on the time grid, we have

$$l = j_l h, \quad r = j_r h, \quad j_r > j_l \geq j(n).$$

We then have

$$\begin{aligned} \Pr[t_{n+1} \in (l = j_l h, r = j_r h], u_{n+1} = u | \tilde{\mathcal{F}}_n] &= \int_l^r \lambda(t, u) e^{-\int_{\Delta_n}^t \bar{\lambda}(s) ds} dt \quad (\text{by (53)}) \\ &= \sum_{j=j_l+1}^{j_r} \frac{\Lambda_j(u)}{\bar{\Lambda}_j} (1 - e^{-h\bar{\Lambda}_j}) e^{-h \sum_{j'=j(n)+1}^{j-1} \bar{\Lambda}_{j'}}, \end{aligned} \quad (64)$$

where the second equality is derived similarly to the proof of Lemma 5.3, making use of Lemma 5.2 under Assumption 5. The probability of having no event till l is

$$\Pr[t_{n+1} > l = j_l h | \tilde{\mathcal{F}}_n] = e^{-h \sum_{j'=j(n)+1}^{j_l} \bar{\Lambda}_{j'}}, \quad (65)$$

which is similar to the time-only case where we replace $\Lambda_{j'}$ with $\bar{\Lambda}_{j'}$ in the expression (30).

5.3 Spatial-temporal Bernoulli process on network

We have derived the discrete time model (61) and (59) under (A3) and Assumption 5. Here, we introduce an equivalent formulation of the model using a spatial-temporal Bernoulli process on the graph \mathcal{V} . Below, we use the boldface notation to emphasize vectors. For example, $\boldsymbol{\mu} = \{\mu(u), u \in \mathcal{V}\} \in \mathbb{R}^V$ and $\boldsymbol{\Lambda}_j = \{\Lambda_j(u), u \in \mathcal{V}\} \in \mathbb{R}^V$ are length- V vectors. We use the boldface \mathbf{x} to denote the vector, and $x(u)$ or x_u stands for the u -th entry. When to emphasize the dependence on parameter θ , we write $\boldsymbol{\Lambda}_j[\theta]$ for the vector and $\Lambda_j[\theta](u)$ for the u -th entry.

Given a trajectory of discrete-time unit-uncertainty event data, define a vector-valued binary sequence $(\mathbf{y}_1, \dots, \mathbf{y}_N)$, and for $t \in [N]$, $\mathbf{y}_t \in \{0, 1\}^V$, where $y_t(u) = 1$ if there exists an event (Δ_i, u_i) s.t. $\Delta_i = I_t$ and $u_i = u$; $y_t(u) = 0$ otherwise. We also define

$$\bar{y}_t := \sum_{u \in \mathcal{V}} y_t(u), \quad t \in [N],$$

and $\bar{y}_t = 1$ indicates that within time interval I_t , there is an event happening somewhere on the network. Using the binary vectors \mathbf{y}_t , (59) is equivalent to

$$\Lambda_t[\theta](u) = \mu(u) + \sum_{i < t} \sum_{u' \in \mathcal{V}} y_i(u') K_{i,t}(u', u), \quad (66)$$

and the log-likelihood (61) can be expressed as

$$\ell = \sum_{t=1}^N \left\{ \bar{y}_t \log \left((1 - e^{-h\bar{\Lambda}_t}) \sum_{u \in \mathcal{V}} y_t(u) \frac{\Lambda_t(u)}{\bar{\Lambda}_t} \right) - (1 - \bar{y}_t) h \bar{\Lambda}_t \right\}. \quad (67)$$

To ensure that the conditional intensity is physical, i.e. $\Lambda_t[\theta](u) > 0$ for any $u \in \mathcal{V}$ and all time t , one can introduce an assumption similar to Assumption 4 and require that, for positive constants $b < B$, $\Lambda_t[\theta](u) \in [b, B]$ for all u and t a.s. when model parameter θ lies in certain domain, including the true intensity $\Lambda_t^*(u)$. As a result, $\boldsymbol{\Lambda}_t^* \in [b, B]^V \subset \mathbb{R}_+^V$ for all t .

Use the vector form of $\boldsymbol{\Lambda}_t$ and \mathbf{y}_t which are in \mathbb{R}^V , we have the following lemma which characterizes the general linear model of predicting y_t given history using $\boldsymbol{\Lambda}_t$, and this gives a counterpart of Lemma 3.3 on network. In this lemma, $\boldsymbol{\Lambda}_t$ refers to the true intensity $\boldsymbol{\Lambda}_t^*$ induced by the true model parameters, which determine the law of the sequence $\{\mathbf{y}_t\}_t$.

Lemma 5.4. *Under Assumption 3(A3) and Assumption 5, and using the formulation of the Bernoulli process \mathbf{y}_t on \mathcal{V} , for any $t \in [N]$, $\boldsymbol{\Lambda}_t \in \sigma\{\mathbf{y}_i, i \leq t-1\}$ and*

$$\mathbb{E}[\mathbf{y}_t | \mathbf{y}_i, i \leq t-1] = \left(\phi(h\bar{\Lambda}_t) \frac{\Lambda_t(u)}{\bar{\Lambda}_t} \right)_{u \in \mathcal{V}} = \Phi(h\boldsymbol{\Lambda}_t), \quad (68)$$

where $\Phi : \mathbb{R}_+^V \rightarrow \mathbb{R}_+^V$ is defined by

$$\Phi(\mathbf{x}) := \frac{1 - \exp\{-\mathbf{x}^T \mathbf{1}\}}{\mathbf{x}^T \mathbf{1}} \mathbf{x}. \quad (69)$$

Because $\mathbf{x} \in \mathbb{R}_+^V$ satisfies $\mathbf{x}^T \mathbf{1} > 0$, (69) is well-defined.

5.4 Influence kernel recovery by VI and GD for networks

Log-likelihood of kernel parameter. Suppose we are given M i.i.d. sequence of observed Bernoulli processes $\{\mathbf{y}_t^{(m)}\}_{m=1}^M$ on the network \mathcal{V} , which are of the same length indexed by $-N' < t \leq N$. For simplicity, we assume that the baseline intensity vector $\boldsymbol{\mu}$ is known and fixed, and we will explain the learning of $\boldsymbol{\mu}$ from data in Section 6.

We denote model parameter θ in (62) as $\theta = \{\boldsymbol{\mu}\} \cup \theta_K$, where θ_K consists of the $NN'V^2$ many influence kernel parameters, again denoted by z . We write $\boldsymbol{\Lambda}_t[z] = \boldsymbol{\Lambda}_t[\boldsymbol{\mu}, z]$, i.e., with $\theta = [\boldsymbol{\mu}, z]$, and similarly for other quantities depending on θ . Next, we introduce the data history vector $\eta_{t,u}$, doubly indexed by t and u and in $\mathbb{R}^{NN'V^2}$, s.t.

$$\langle \eta_{t,u}, z \rangle = \sum_{i=t-N'}^{t-1} \sum_{u' \in \mathcal{V}} y_i(u') K_{i,t}(u', u). \quad (70)$$

This allows (66) to be represented as $\Lambda_t[z](u) = \mu(u) + \langle \eta_{t,u}, z \rangle$, and $\bar{\Lambda}_t[z] = \sum_{u \in \mathcal{V}} \Lambda_t[z](u)$. With this notation, by (67), the log-likelihood of parameter θ on the m -th sequence can be written as

$$\ell^{(m)}[z] = \sum_{t=1}^N \left\{ \bar{y}_t^{(m)} \log \left((1 - e^{-h\bar{\Lambda}_t^{(m)}[z]}) \sum_{u \in \mathcal{V}} y_t^{(m)}(u) \frac{\Lambda_t^{(m)}[z](u)}{\bar{\Lambda}_t^{(m)}[z]} \right) - (1 - \bar{y}_t^{(m)}) h \bar{\Lambda}_t^{(m)}[z] \right\}, \quad (71)$$

$$\Lambda_t^{(m)}[z](u) = \mu(u) + \langle \eta_{t,u}^{(m)}, z \rangle, \quad \bar{\Lambda}_t^{(m)}[z] = \sum_{u \in \mathcal{V}} \Lambda_t^{(m)}[z](u), \quad (72)$$

and the total likelihood is averaged over the M trajectories.

VI scheme on network. With the mapping Φ defined as in (69), we can again conceptually define the per-trajectory L^2 loss as

$$\ell_{\text{VI}}^{(m)}(z) = \frac{1}{2h} \sum_{t=1}^N \|\Phi(h\boldsymbol{\Lambda}_t^{(m)}[z]) - \mathbf{y}_t^{(m)}\|_2^2.$$

For a vector $y \in \mathbb{R}^V$, we use both bracket $y(u)$ or subscript y_u to denote the u -th entry of the vector. Following the stochastic update scheme in Section 4.3, the per-trajectory VI field can be written as

$$\begin{aligned} \hat{G}^{(m)}[z] &= \sum_{t=1}^N \sum_{u \in \mathcal{V}} \left(\Phi(h\boldsymbol{\Lambda}_t^{(m)}[z]) - \mathbf{y}_t^{(m)} \right)_u \eta_{t,u}^{(m)} \\ &= \sum_{t=1}^N \sum_{u \in \mathcal{V}} \left(\phi(h\bar{\Lambda}_t^{(m)}[z]) \frac{\Lambda_t^{(m)}[z](u)}{\bar{\Lambda}_t^{(m)}[z]} - y_t^{(m)}(u) \right) \eta_{t,u}^{(m)}. \end{aligned} \quad (73)$$

We update the solution z_k at the k -th iteration by looping over the training trajectories similarly to before. It is possible to extend the recovery guarantee theory in Section 4.3 to the network case, which we leave for future work.

GD scheme on network. The GD dynamic solves for the MLE based on the likelihood model (71)(72). Again, we focus on the stochastic GD update, and by differentiating (71), the per-trajectory gradient field can be computed directly to be

$$\hat{F}^{(m)}(z) = \sum_{t=1}^N \sum_{u \in \mathcal{V}} \left(\frac{h(\phi(h\bar{\Lambda}_t^{(m)}[z]) - \bar{y}_t^{(m)})}{\phi(h\bar{\Lambda}_t^{(m)}[z])} + \frac{\bar{y}_t^{(m)}}{\bar{\Lambda}_t^{(m)}[z]} - \frac{y_t^{(m)}(u)}{\Lambda_t^{(m)}[z](u)} \right) \eta_{t,u}^{(m)}, \quad (74)$$

where we used that when $y_t(u) = 1$, $\sum_{u' \in \mathcal{V}} y_t(u') \Lambda_t(u') = \Lambda_t(u)$ because when time t is even, then only one node can have an event on it.

We see that (74) contains terms like $y_t(u)/\Lambda_t(u)$ which will be $\Lambda_t(u)^{-1}$ at an event location u , and thus can be large when $\Lambda_t(u)$ is small. In comparison, the VI field in (73) does not have such terms (the ratio $\Lambda_t(u)/\bar{\Lambda}_t$ is always between 0 and 1, which will not cause divergent magnitude). This suggests that the VI training dynamic can be more stable than the GD dynamic, echoing the same phenomenon in the time-only case (see comments at the end of Section 4.2).

Special structures for spatial-temporal kernels. Similar to Section 4.4, one can incorporate special structures of the kernel structure into the inference procedure when such prior knowledge is available. For example, assuming time stationarity, one will have a time-invariant kernel $K_{i,j}(u', u) = \Psi_{i,j-i}(u', u) = \psi_{j-i}(u', u)$, $\forall u, u' \in \mathcal{V}$, and there are $N'V^2$ many kernel parameters to learn from data. The likelihood model (71)(72) still holds, and the VI and GD optimization methods can also be extended.

In the network case, because the spatial-temporal kernel parameters K or Ψ are four-way tensors, there are different ways to impose low-rank structures on the kernel. Motivated by the underlying temporal continuity of the influence kernel function, as has been explained in Section 4.4, one can expect approximate low-rankness of the discrete kernel over time, e.g., the matrix $[\Psi_{i,l}(u', u)]_{i,l}$ for each pair of (u', u) . As an additional simplification, we concatenate these matrices over all pairs of (u', u) to form a tall matrix of size $(N - N' + 1)V^2 \times N'$, using the middle-chunk trick in Section 4.4, and impose low-rankness on the resulting matrix.

The above two techniques exploit the temporal structures of the kernel, and it is also possible to impose constraints or regularizations based on the spatial information, i.e. graph topology of the network. In the real data application of this work, to discover a network structure using the Sepsis-Associated Derangements (SADs) data (Section 7), we do not assume any prior knowledge of the network where graph nodes represent medical status. Instead, we will use the inferred spatial-temporal kernel from event data to reveal influence relations among the nodes. Thus, in this work, we do not explore any spatial structure or regularization of the kernel, which is possible and would certainly be useful in other application scenarios.

6 Algorithm

The estimation methods using VI and GD have been introduced for the time-only case in Section 4 and extended to the on-network case in Section 5.4. We provide additional algorithmic details in this section.

6.1 Time-only case

Stochastic optimization by batches. We theoretically proved in Section 4.3 the (in-expectation) convergence of the stochastic scheme (39), where one training trajectory is used in each step of updating the model parameter, i.e., the batch size is one. This choice is for the convenience of exposition for the theory. In practice, the batch size in a stochastic optimization algorithm balances between the efficiency of parameter adaptation versus random fluctuation of the solution. When the batch size is small, the solution can develop large variations across batches.

In our algorithm, we use a finite batch size M_B , which can be up to a few hundred. In each step of parameter update, we load M_B many training trajectories, called a “batch” and denoted by Y_B . The batches are non-overlapping and loop over the training set, and when one pass of the training set is finished, it is called an “epoch”. We random shuffle the training set indices at the beginning

Algorithm 1: Stochastic batch-based training for time-only case

Input : Training trajectories $\{y_t^{(m)}\}_{m=1}^M$, μ_0 as initial value of μ ; Parameters: intensity lower bound b , barrier weight δ_b ; batch size M_B , maximum number of epochs k_{\max} , learning rate schedule $\{\gamma_k\}_k$; Optional: singular value threshold τ_{SVD} , smoothness weight δ_s

Output: Learned kernel θ_K and baseline μ

- 1 Initialize kernel $\theta_K \leftarrow 0$ and baseline $\mu \leftarrow \mu_0$
- 2 **for** $k = 1, \dots, k_{\max}$ **do**
- 3 **while** loop over the batches **do**
- 4 $\theta \leftarrow [\mu, \theta_K]$
- 5 Load M_B many training trajectories to form batch $Y_B = \{y^{(m)}\}_m$
- 6 Compute intensities $\Lambda_t^{(m)}(\theta)$ in (36) at $t = 1, \dots, N$ for each $y^{(m)}$ in Y_B , and let $b^{(m)} \leftarrow \min_{1 \leq t \leq N} \Lambda_t^{(m)}$
- 7 Split $Y_B = Y_{B,1} \cup Y_{B,2}$, where $y^{(m)}$ in $Y_{B,1}$ if $b^{(m)} < b$, and otherwise in $Y_{B,2}$
- 8 **if** using VI update **then**
- 9 $g_B \leftarrow \frac{1}{M_B} \sum_{y^{(m)} \in Y_{B,2}} \hat{G}^{(m)}(\theta)$, $\hat{G}^{(m)}$ as in (38)
- 10 **else if** using GD update **then**
- 11 $g_B \leftarrow \frac{1}{M_B} \sum_{y^{(m)} \in Y_{B,2}} \hat{F}^{(m)}(\theta)$, $\hat{F}^{(m)}$ as in (37)
- 12 **end**
- 13 **if** $Y_{B,1}$ not empty **then**
- 14 $g_B \leftarrow g_B + \delta_b \sum_{y^{(m)} \in Y_{B,1}} \partial_{\theta_K} B^{(m)}(\theta)$, $B^{(m)}$ as in (76)
- 15 **end**
- 16 Update $\theta_K \leftarrow \theta_K - \gamma_k g_B$
- 17 Solve $\tilde{\mu}$ as root of (75) on Y_B using bisection search
- 18 Update $\mu \leftarrow 0.9\mu + 0.1\tilde{\mu}$
- 19 **end**
- 20 (Optional) **if** do smoothness regularization of kernel **then**
- 21 $\theta_K \leftarrow \theta_K - \gamma_k \delta_s \partial_{\theta_K} S(\theta_K)$, S as in (77)
- 22 **end**
- 23 **end**
- 24 (Optional) **if** do low-rank truncation of kernel **then**
- 25 Rearrange entries in θ_K into Ψ , and $\Psi' \leftarrow \Psi_{(N'+1):N, 1:N'}$
- 26 $r \leftarrow$ number of singular values of Ψ' larger than τ_{SVD}
- 27 $V \leftarrow$ first r right singular vectors of Ψ'
- 28 $\Psi \leftarrow \Psi V V^\top$, and rearrange Ψ into θ_K
- 29 **end**
- 30 **return** μ, θ_K

of each epoch. Following the convention of stochastic optimization literature, the parameter update step size γ_k is called “learning rate. Instead of decreasing γ_k per batch (with batch size one) as theoretically in Theorem 4.5, we set a learning rate schedule indexed by the epochs till the maximum number of epochs. The stochastic optimization algorithm is summarized in Algorithm 1.

Inference of baseline intensity μ . To be able to infer the baseline μ from data, our idea is to eliminate the variable μ in the process of learning θ_K , making use of the first-order condition of the

log-likelihood objective. Specifically, from (35) we have that, with $\theta = [\mu, \theta_K]$,

$$\partial_\mu \ell^{(m)}(\theta) = \sum_{t=1}^N h \left(\frac{y_t^{(m)}}{1 - e^{-h\Lambda_t^{(m)}(\theta)}} - 1 \right),$$

and for fixed θ_K , one can solve for the value of μ by the following 1D non-linear equation

$$0 = \sum_{m, y^{(m)} \in Y_B} \partial_\mu \ell^{(m)}(\theta) = \sum_{m, y^{(m)} \in Y_B} \sum_{t=1}^N h \left(\frac{y_t^{(m)}}{1 - e^{-h\Lambda_t^{(m)}(\theta)}} - 1 \right). \quad (75)$$

The equation can be solved by *bisection search* due to the monotonicity of the function $1 - e^{-h\Lambda_t^{(m)}(\theta)}$ with respect to μ , recalling that $\Lambda_t^{(m)}(\theta) = \mu + \langle \eta_t^{(m)}, \theta_K \rangle$.

Strictly speaking, the first-order condition corresponds to averaging over all the M training trajectories, and in (75) we use the batch average to approximate solving for μ given the current θ_K and update the baseline more diligently. In our algorithm, we update μ by a convex combination of the current μ with the solution $\tilde{\mu}$ from the batch Y_B so as to implement an average over the batches. The initial value μ_0 of μ is set to be the empirical frequency of having an event averaged over the time horizon, i.e., $\mu_0 = \sum_{m=1}^M n^{(m)} / (MNh)$ where $n^{(m)} = \sum_{t=1}^N y_t^{(m)}$ is the count of events on $1 \leq t \leq N$ of the m -th trajectory. We observe the numerical convergence of this scheme to learn μ in practice, see Figure A.1b.

Constraint and regularization of the kernel. Motivated by Assumption 4(ii), we enforce the lower-boundedness of the model intensity $\Lambda_t^{(m)} \geq b$ for all $1 \leq t \leq N$ and all training trajectories, where the minimum intensity threshold b is an algorithmic parameter. We introduce a (per-trajectory) barrier function $B^{(m)}$ to penalize the violations, defined as

$$B^{(m)}(\theta) = \sum_{t=1}^N \mathbf{1}_{\{\Lambda_t^{(m)}(\theta) < b\}} l_b(\Lambda_t^{(m)}(\theta)), \quad (76)$$

and is weighted by a penalty strength factor δ_b . The barrier function $l_b : \mathbb{R} \rightarrow \mathbb{R}$ is differentiable, and then $\partial_{\theta_K} B^{(m)}(\theta) = \sum_{t=1}^N \mathbf{1}_{\{\Lambda_t^{(m)}(\theta) < b\}} l'_b(\Lambda_t^{(m)}(\theta)) \eta_t^{(m)}$. In experiments, we find that several choices of l_b can work well, and in our experiments, we use (i) log-barrier $l_b(x) = -b \log(x/b)$ or (ii) quadratic barrier $l_b(x) = \frac{1}{0.2b}(x - b)^2$.

The underlying continuity of the kernel function suggests the low-rankness of the kernel matrix, as has been explained in Section 4.4. To leverage such prior structural information, we can apply a low-rank truncation of the learned kernel matrix by the stochastic optimization using the submatrix trick in Section 4.4, see the end of Algorithm 1. We only keep singular vectors for which the singular value is greater than τ_{SVD} , and this threshold is an algorithmic parameter.

Another optional regularization of the kernel matrix is by regularizing the variation of the kernel matrix Ψ across time. Specifically, writing θ_K into the form of matrix Ψ , one can adopt the smoothness penalty

$$S(\theta_K) = \frac{1}{2h^2} \left(\sum_{i=-N'+1}^{N-1} \sum_{l=1}^{N'} (\Psi_{i,l} - \Psi_{i+1,l})^2 + \sum_{i=-N'+1}^N \sum_{l=1}^{N'-1} (\Psi_{i,l} - \Psi_{i,l+1})^2 \right) \quad (77)$$

weighted by a strength factor δ_s . In our algorithm, we update the kernel using the gradient of $\partial_{\theta_K} S$ after each epoch. The choices of the parameters b , δ_b , δ_s together with the optimization hyperparameters depend on the problem and will be detailed in our experiments (Appendix D).

6.2 On-network case

The methodology in Section 6.1 can be extended to the on-network model, implementing the VI and GD inference as has been introduced in Section 5.4. The setup of batch-based stochastic optimization, the constraint enforcement, and the regularization of the kernel matrices are similar, and a main difference lies in the learning of baseline vector $\boldsymbol{\mu}$, which we again utilize the first-order condition. This is summarized in Algorithm 2 in the Appendix, and we give technical details of the extensions below.

Similar to (75), we propose to solve for $\boldsymbol{\mu}$ given kernel θ_K by requiring the derivative of the log-likelihood with respect to each $\mu(u)$ to vanish. That is, with $\theta = [\boldsymbol{\mu}, \theta_K]$ and again averaged on a batch of trajectories Y_B ,

$$\begin{aligned} 0 &= \sum_{m, \mathbf{y}^{(m)} \in Y_B} \frac{\partial \ell^{(m)}[\theta]}{\partial \mu(u)} \\ &= \sum_{m, \mathbf{y}^{(m)} \in Y_B} \sum_{t=1}^N \left(h \left(\frac{\bar{y}_t^{(m)}}{1 - e^{-h\bar{\Lambda}_t^{(m)}[\theta]}} - 1 \right) - \frac{\bar{y}_t^{(m)}}{\bar{\Lambda}_t^{(m)}[\theta]} + \frac{y_t^{(m)}(u)}{\Lambda_t^{(m)}[\theta](u)} \right), \quad \forall u \in \mathcal{V}, \end{aligned}$$

and we recall that $\Lambda_t^{(m)}[\theta](u) = \mu(u) + \langle \eta_{t,u}^{(m)}, \theta_K \rangle$. These V equations are non-linear because all three terms inside the summation involve $\boldsymbol{\mu}$ through $\bar{\Lambda}_t^{(m)}$ and $\Lambda_t^{(m)}$. To simplify the algorithm, we propose a Gauss-Seidel-type iteration: given the current $\boldsymbol{\mu}$ and θ_K fixed, we solve for $\tilde{\boldsymbol{\mu}}(u)$ for each $u \in \mathcal{V}$ by the equation

$$0 = \sum_{m, \mathbf{y}^{(m)} \in Y_B} \sum_{t=1}^N \left(h \left(\frac{\bar{y}_t^{(m)}}{1 - e^{-h\bar{\Lambda}_t^{(m)}[\boldsymbol{\mu}, \theta_K]}} - 1 \right) - \frac{\bar{y}_t^{(m)}}{\bar{\Lambda}_t^{(m)}[\boldsymbol{\mu}, \theta_K]} + \frac{y_t^{(m)}(u)}{\tilde{\boldsymbol{\mu}}(u) + \langle \eta_{t,u}^{(m)}, \theta_K \rangle} \right). \quad (78)$$

These V equations are then decoupled, each one is a one-dimensional non-linear equation and bisection search can be applied due to the monotonicity with respect to $\tilde{\boldsymbol{\mu}}(u)$. After solving the vector $\{\tilde{\boldsymbol{\mu}}(u)\}_{u \in \mathcal{V}}$ on a batch, we do a convex combination with the current $\boldsymbol{\mu}$, same as before. The vector $\boldsymbol{\mu}$ is initialized by $\mu_0(u) = \sum_{m=1}^M n^{(m)}(u)/(MNh)$ where $n^{(m)}(u) = \sum_{t=1}^N y_t^{(m)}(u)$ is the count of events happening at location u along the m -th trajectory. We empirically observe the convergence of our iteration scheme to learn $\boldsymbol{\mu}$ as shown in Figure A.4b.

We also extend the constraints and regularizations on the time-only kernel to the spatial-temporal kernel on a network. Specifically, the penalty to enforce lower boundedness of the model intensities applies to each node, i.e.

$$B^{(m)}[\theta] = \sum_{t=1}^N \sum_{u \in \mathcal{V}} \mathbf{1}_{\{\Lambda_t^{(m)}[\theta](u) < b\}} l_b(\Lambda_t^{(m)}[\theta](u)). \quad (79)$$

The optional low-rank truncation is applied to the tall concatenated Ψ matrix across all pairs of nodes, as has been explained in Section 5.4. The optional smoothness regularization is by applying the penalty S in (77) to the time-only kernel on each pair of nodes.

Depending on the problem, e.g., the size of the problem, namely N , N' , and the graph size V , as well as the inference approach (GD or VI), we may need different parameters b , δ_b , δ_s as well as optimization hyperparameters like batch size and learning rate schedule. The choices will be detailed in the experiments (Appendix D).

7 Experiments

In this section, we compare the proposed model with various baselines on simulated and real data.

7.1 Simulated event data: Time-only

Dataset. For time-only event data, we set a time horizon $[-\tau_{\max}, T]$ with $\tau_{\max} = 4$ and $T = 16$. The model adopts a latent influence kernel function $k(t', t)$ defined as

$$k(t', t) = \sum_{j=1}^{13} 0.3(2)^{-j} (\cos(2 + 1.3\pi(j+1)((t' - 9)/15)) + 0.6)e^{-8((t-t')j)^2/25}, \quad t > t', \quad (80)$$

which, after specifying N and N' , will induce a kernel matrix K in (23). In this example, the influence kernel matrix K will have both positive and negative entries, indicating that the history may elicit both excitatory and inhibitory effects between events. Additionally, the influence kernel is time-varying, indicating that these effects are non-stationary over time.

We use two types of discrete time grids: (a) $N' = 8, N = 32$, and (b) $N' = 80, N = 320$. The corresponding kernel matrices are visualized in Figure 4a and Figure 6a respectively in the form of Ψ defined as in (32). We use $\mu = 0.2$, and the event data are simulated by the law of a Bernoulli process as introduced in Section 3.3. The training and testing sets consist of 16,000 and 500 trajectories, respectively.

Method. In the experimental results, we refer to our model as the Time Uncertain Latent Influence Kernel (TULIK) point processes, and the model estimated using VI and GD (following Algorithm 1 as introduced in Section 6.1) are referred to as TULIK-VI and TULIK-GD, respectively. The choice of

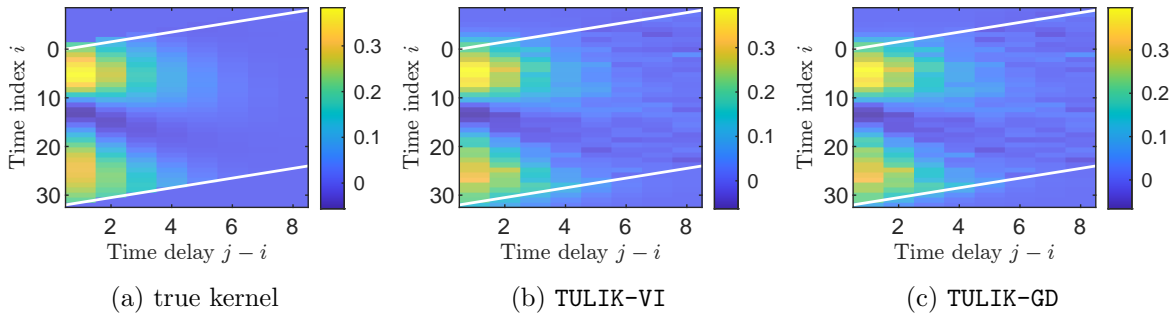


Figure 4: Recovered kernels on simulated time-only event data with kernel function defined in (80), $N' = 8$ and $N = 32$. (a) The true kernel. (b) The kernel recovered by TULIK-VI. (c) The kernel recovered by TULIK-GD. The white lines indicate the estimable parameters.

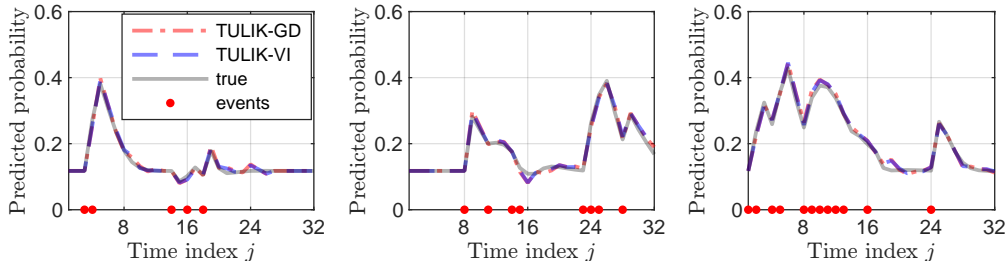


Figure 5: The probability predictions on three randomly selected testing sequences. Data is the simulated time-only event data with kernel function defined in (80), $N' = 8$ and $N = 32$.

Table 1: Relative Errors (REs) of learned μ , kernel matrix, and probability predictions, on simulated time-only event data with the kernel function defined in (80), $N' = 8$ and $N = 32$. We report means of REs over 10 replicas, and standard deviations are in parentheses. For probability predictions, the best performance is in boldface. Note that μ is a scalar in the time-only example and its ℓ_1 , ℓ_2 , and ℓ_∞ errors are the same.

		time-only event data with discrete time grids $N' = 8$ and $N = 32$								
RE $\times 10^{-2}$	μ		kernel		prediction					
	TULIK-VI	TULIK-GD	TULIK-VI	TULIK-GD	TULIK-VI	TULIK-GD	GLM-L	GLM-S	HP-E	
ℓ_1	0.40 (0.38)	0.47 (0.41)	16.37 (0.82)	18.39 (0.86)	2.85 (0.11)	3.20 (0.15)	3.93 (0.19)	6.13 (0.19)	37.08 (0.65)	
ℓ_2	–	–	12.07 (0.70)	13.46 (0.66)	3.96 (0.16)	4.43 (0.20)	5.25 (0.21)	7.99 (0.14)	53.06 (1.14)	
ℓ_∞	–	–	11.26 (1.40)	12.35 (1.32)	6.02 (0.35)	6.73 (0.38)	8.09 (0.41)	12.85 (0.30)	92.83 (2.49)	

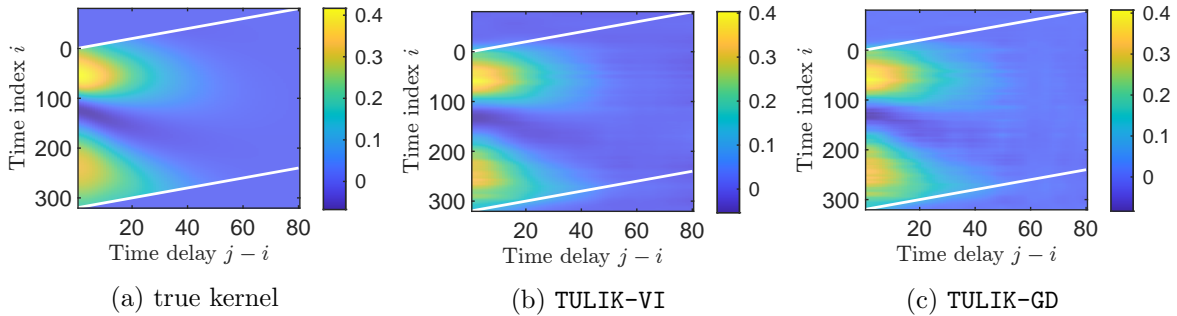


Figure 6: Recovered kernels on simulated time-only event data with kernel function defined in (80), $N' = 80$ and $N = 320$. Same plots as in Figure 4. The recovered kernel is after a low-rank truncation.

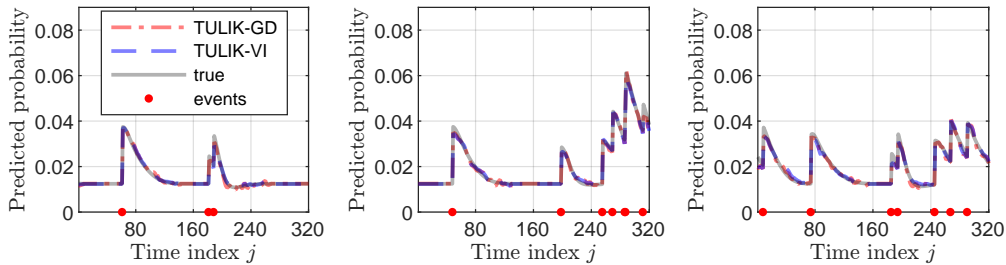


Figure 7: Same plots as in Figure 5. Data is the simulated time-only event data with kernel function defined in (80), $N' = 80$ and $N = 320$.

training hyperparameters is detailed in Appendix D.1.1. The training dynamic on one training set, including the evolution of the training (negative) log-likelihood and the convergence of the learned μ are illustrated in Figure A.1.

For comparison, we consider three alternative baselines: (1) Generalized Linear Model (GLM) [15] with linear link function (GLM-L), where the link function is an identity function with range $[0, 1]$; (2) GLM with Sigmoid link function (GLM-S); (3) Continuous-time Hawkes Process with Exponential kernel (HP-E) [11–13], see more in Section 2.1. The implementation details of the alternative baselines can be found in Appendix D.1.3.

Table 2: Relative Errors (REs) of learned μ , kernel matrix, and probability predictions, on simulated time-only event data with the kernel function defined in (80), $N' = 80$ and $N = 320$. The format are the same as in Table 1.

		time-only event data with discrete time grids $N' = 80$ and $N = 320$							
RE $\times 10^{-2}$	μ		Kernel		Prediction				
	TULIK-VI	TULIK-GD	TULIK-VI	TULIK-GD	TULIK-VI	TULIK-GD	GLM-L	GLM-S	HP-E
ℓ_1	1.46 (0.80)	0.72 (0.37)	14.49 (0.53)	18.23 (0.67)	3.34 (0.23)	3.89 (0.19)	37.11 (0.59)	27.96 (0.49)	72.88 (1.74)
ℓ_2	–	–	11.58 (0.50)	13.39 (0.52)	4.50 (0.19)	5.31 (0.25)	51.65 (0.48)	39.79 (0.79)	149.82 (5.44)
ℓ_∞	–	–	17.50 (1.52)	17.04 (2.27)	8.64 (0.59)	9.44 (0.50)	98.82 (0.91)	101.33 (2.57)	393.29 (17.25)

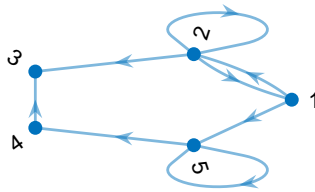


Figure 8: The visualization for the network structure of the on-network event data in Section 7.2.

Results. For data with $N' = 8$ and $N = 32$, both TULIK-VI and TULIK-GD can learn the true model parameters (μ and kernel matrix) well, resulting in good prediction performance, as shown quantitatively in Table 1. The proposed TULIK models outperform the other three baselines, where TULIK-VI gains slightly better performance than TULIK-GD. The recovered kernel matrices are plotted in Figure 4, showing a good agreement with the true kernel. The predicted probability is also close to the ground truth, as reflected by the almost overlapping curves in Figure 5.

For the data with $N' = 80$ and $N = 320$, which results in much higher dimensional trainable parameters, the proposed TULIK model can still achieve reasonable recovery of kernel matrices and μ 's and accurate probability predictions. Figure 6 shows that both TULIK-VI and TULIK-GD produce correct shapes and magnitudes of kernel matrices, where we applied low-rank truncation to the learned kernel matrix. Figure 7 visualizes the probability predictions in good agreement with the ground truth. From the quantitative errors in Table 2, our proposed model again achieves the best relative prediction errors, and VI slightly outperforms GD.

Example of a stationary process. As has been introduced in Section 4.4, the proposed TULIK model can be applied to stationary processes with time uncertainty, where the kernel is time-invariant. This is a special case of the more general time-varying kernel. We provide experiments on such a simplified case in Appendix D.2. The results show that the proposed approach successfully recovers the model parameters and outperforms the alternative baselines.

7.2 Simulated event data on networks

Dataset. For the on-network event data, we set a time horizon $[-\tau_{\max}, T]$ with $\tau_{\max} = 0.8$ and $T = 3.2$. The network has $V = 5$ nodes, in which 8 pairs of successors and predecessors are randomly sampled from \mathcal{V} to form 8 directed edges. The network structure is visualized in Figure 8. For a

directed edge $u' \rightarrow u$, the marginal kernel (temporal pattern) is defined as

$$k(t', t; u', u) = 0.35 (\cos(\omega_{u',u}(t+2)) + 0.75) e^{-20(t-t'-h_{u',u})^2}, \quad (81)$$

where $\omega_{u',u}$ independently follows $\text{Uniform}(2, 6)$ and $h_{u',u}$ is independently drawn from $\text{Uniform}(0, 0.2)$. Given $N' = 8$ and $N = 32$, we can induce the four-way kernel tensor Ψ as in (63) and visualize it in Figure 9a. The non-zero block matrix on u' -th row and u -th column corresponds to a directed edge $u' \rightarrow u$. The zero block matrices indicate disconnected pairs of nodes.

Given the kernel and $\mu(u)$ independently sampled from $\text{Uniform}(0.25, 0.35)$ for $u \in \mathcal{V}$, we can generate on-network Bernoulli process data as in Section 5.3. The training data and testing data contain 40000 and 500 trajectories, respectively.

Method. We train the proposed model using Algorithm 2 (in Appendix) as introduced in Section 6.2. The choice of training hyperparameters is discussed in Appendix D.3.1. The convergence of the training (negative) log-likelihood and the learned μ vector is illustrated in Figure A.4. We compare the proposed method with the baselines, including GLM-L, GLM-S, and HP-E. The implementation details of the alternative baselines in the on-network setting are given in Appendix D.3.3.

Results. Both TULIK-VI and TULIK-GD can learn the vector μ and the kernel tensor, leading to accurate prediction as quantitatively revealed in Table 3. Similar to the time-only examples, the proposed TULIK models yield smaller prediction errors than the other baselines, where TULIK-VI

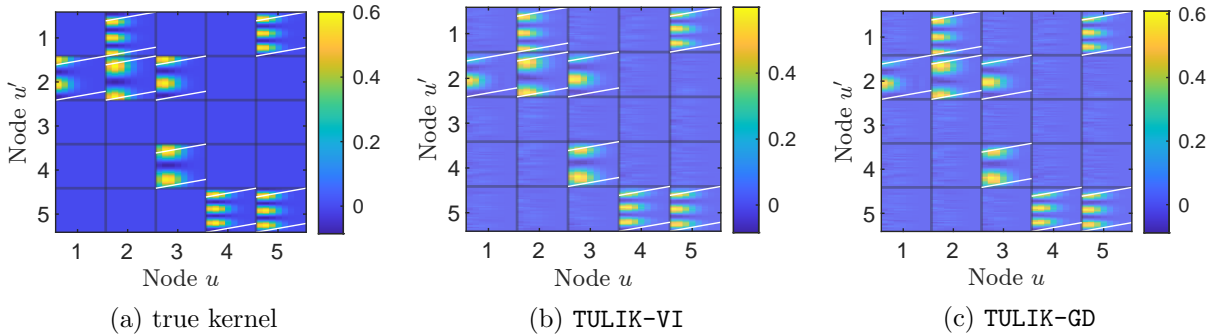


Figure 9: Recovered kernel tensors on simulated on-network event data with kernel function defined in (81), $V = 5$, $N' = 8$ and $N = 32$. (a) The true kernel. (b) The kernel recovered by TULIK-VI. (c) The kernel recovered by TULIK-GD. The learned kernels are after low-rank truncation. The (u', u) -th block in the plot shows the kernel matrix $[\Psi_{i,l}(u', u)]_{i,l}$, for $u', u = 1, \dots, 5$. The white slashes box out the trainable parameters of the kernel matrices corresponding to the directed edges.

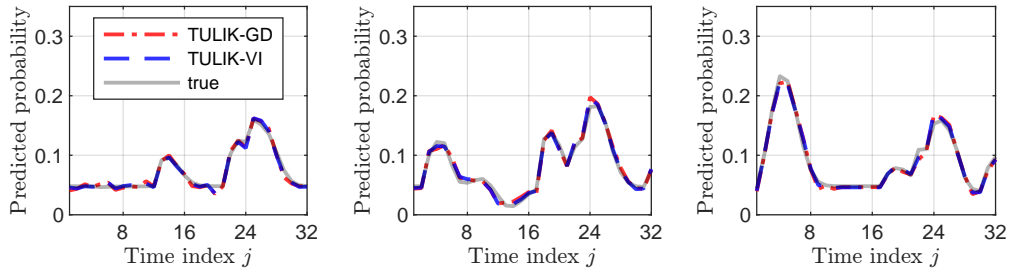


Figure 10: The probability predictions on 3 randomly selected testing sequences on one node (node 3 in the graph in Figure 8). Data is the simulated on-network event data with kernel function defined in (81), $V = 5$, $N' = 8$, and $N = 32$.

Table 3: Relative Errors (REs) of learned μ , kernel tensor, and probability predictions, on simulated on-network event data with the kernel function defined in (81), $V = 5$, $N' = 8$, and $N = 32$. We report means of REs over 10 replicas, and standard deviations are in parentheses. For probability predictions, the best performance is in boldface.

RE $\times 10^{-2}$		on-network event data with discrete time grids $N' = 8$ and $N = 32$								
		μ		Kernel		Prediction				
		TULIK-VI	TULIK-GD	TULIK-VI	TULIK-GD	TULIK-VI	TULIK-GD	GLM-L	GLM-S	HP-E
ℓ_1	7.28	6.04	19.11	21.07	6.36	7.47	9.29	10.29	31.55	
	(0.52)	(0.57)	(0.57)	(0.44)	(0.09)	(0.09)	(0.11)	(0.11)	(0.45)	
ℓ_2	7.40	6.19	13.49	14.70	7.42	8.76	11.32	13.94	45.97	
	(0.56)	(0.60)	(0.33)	(0.24)	(0.09)	(0.09)	(0.12)	(0.14)	(0.41)	
ℓ_∞	8.15	7.09	17.22	17.22	9.62	11.09	15.01	25.97	72.12	
	(0.82)	(0.85)	(2.00)	(2.16)	(0.07)	(0.19)	(0.15)	(0.53)	(0.33)	

is slightly better than TULIK-GD. After optimization loops, we apply low-rank truncation to the matrix Ψ , and the learned kernel tensors are visualized in Figure 9. It can be seen that the kernel is well recovered, and in particular, the learned kernel reveals the correct causal network: when (u', u) is a missing (directed) edge in the network (Figure 8), the corresponding block in the learned kernel also takes almost zero values. The predicted probability is also consistent with the ground truth, as shown in Figure 10 (the prediction is successful on all the nodes, where the plots on one node are shown).

8 Real data

8.1 Sepsis-Associated-Derangements (SADs) data

Dataset. We consider the data to be publicly available through the 2019 PhysioNet Challenge [28], which consists of hospitalization records of Intensive Care Unit (ICU) patients. Each patient record includes three main types of variables: vital signs, laboratory (lab) measurements, and demographic information. The goal is to use this data to predict the onset of sepsis—a condition that arises when the body’s response to infection causes tissue damage, organ failure, or death, and can quickly

Table 4: Selected 13 medical indices in SADs data

Node	Abbreviation	Full Name
1	RI Kernel	Renal Injury
2	EI	Electrolyte Imbalance
3	OCD	Oxygen Carrying Dysfunction
4	Shock	Shock
5	DCO	Diminished Cardiac Output
6	Cl	Coagulopathy
7	Chl	Cholestasis
8	HI	Hepatocellular Injury
9	OD(Lab)	Oxygenation Dysfunction (Lab)
10	Inf(Lab)	Inflammation (Lab)
11	OD(vs)	Oxygenation Dysfunction (vital sign)
12	Inf(vs)	Inflammation (vital sign)
13	Sepsis	Sepsis

Table 5: Sepsis prediction: True Positive Rate (TPR), True Negative Rate (TNR), and Balanced Accuracy (BA) from TULIK-VI. The standard deviations of TPR, TNR, and BA over 10 training replicas are in parentheses. The highest metrics are bolded. The training data and testing data consist of 1070 and 71 patient trajectories, respectively.

	TULIK-VI	TULIK-VI (Stationary)	GLM-L	GLM-S	HP-E
TPR	0.6842 (0.0000)	0.4632 (0.0211)	0.5789 (0.0000)	0.6316 (0.0000)	0.0000 (0.0000)
TNR	0.6904 (0.0058)	0.4519 (0.0197)	0.5769 (0.0000)	0.6731 (0.0000)	0.0192 (0.0000)
BA	0.6873 (0.0029)	0.4575 (0.0203)	0.5779 (0.0000)	0.6523 (0.0000)	0.0096 (0.0000)

become life-threatening [32].

We use a processed version of this dataset, referred to as SADs [35–37], which was created by grouping all raw observations—including vital signs and lab measurements—into 13 medical indices using a standard procedure [1]. These indices represent common physiological derangements associated with sepsis and are treated as nodes in our graph. Table 4 lists the abbreviations and names of the indices. Vital signs are recorded hourly, introducing a natural one-hour time uncertainty in the data. Lab test results are typically returned within 24 hours, leading to greater time uncertainty; that is, the test result indicates the patient’s condition within 24 hours around the test time. For simplicity, we assume the test time uncertainty is also 1 hour. Appendix D.4.1 contains details on data pre-processing.

Given the 13 medical indices, the processed SAD data can be viewed as a point process on a network with $V = 13$ nodes, with a time uncertainty of 1 hour. Each patient’s data trajectory is a Boolean process on this network, which we refer to as a “signal” that takes values 0 or 1 at each node ($y_t(u) \in \{0, 1\}$). We consider the 24 hours following ICU admission and set the influence time lag, τ_{\max} , to 4 hours. As a result, the time horizon is $[-\tau_{\max}, T] = [-4, 20]$, covering a total of 24 hours. The time grid has $N = 20$ and $N' = 4$, with unit uncertainty of one hour.

The node “Sepsis” marks the onset of sepsis for each patient, according to the Sepsis-3 definition. For time points more than 6 hours before sepsis onset, the observation on the sepsis node is always 0; after sepsis onset, the observation remains positive. To support early prediction of sepsis onset, the positive labels are shifted 6 hours earlier, meaning that prediction within 6 6-hour period before and after the initial onset of sepsis is meaningful, consistent with the definition in Physionet Challenge [28].

In the experiments below, the processed dataset comprises 1,141 patient records, all of whom were diagnosed with sepsis, with varying onset times. We randomly select 1,070 trajectories for training and 71 trajectories for testing.

Method. We use TULIK-VI on the SADs dataset, as it exhibits more stable training behavior than TULIK-GD in our case. As in Section 7.2, we compare the proposed model with baseline methods, including GLM-L, GLM-S, and HP-E. Experimental details are provided in Appendices D.4.3 and D.4.2.

Results. The performance of all methods is reported in Table 5. We evaluate True Positive Rate (TPR), True Negative Rate (TNR), and Balanced Accuracy (BA), on the testing data. These evaluation metrics are standard for sepsis prediction [28]. As shown in the table, TULIK-VI consistently outperforms the baseline methods.

In particular, TULIK, which allows for non-stationary modeling, significantly outperforms its stationary counterpart, indicating that the sepsis data likely contain substantial non-stationarity,

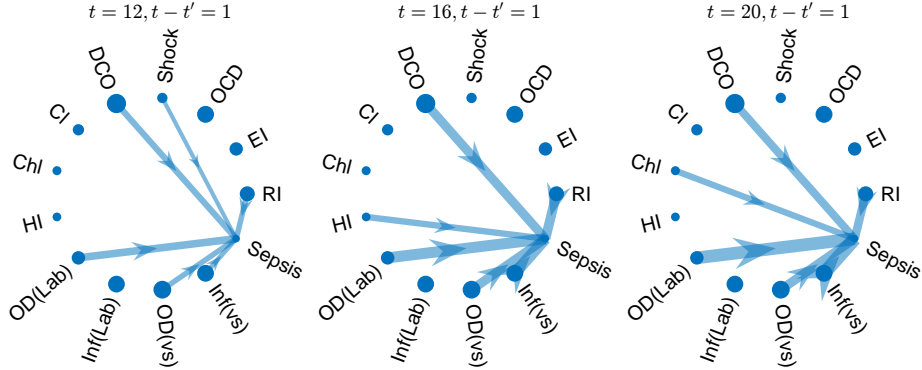


Figure 11: Temporally evolving influence networks. For clarity of visualization, only the top five strongest edges are shown. The time lag $t - t'$ is fixed at 1, corresponding to one-hour effects. The future time t progresses from 12 to 20 in increments of 4. Node radii are proportional to their baseline intensities. Blue arrows indicate excitation effects, with arrow widths scaled to reflect their magnitudes. Marker sizes and line widths are consistent across all plots.

which our model effectively captures. TULIK, with its modeling of time uncertainty and flexible triggering pattern modeling, also outperforms methods that do not account for time uncertainty, such as GLM-L and GLM-S, which use standard link functions, and continuous time HP-E, which employs a parametric exponential decaying triggering kernel. These results highlight the importance of incorporating both time uncertainty and nonparametric triggering structures in modeling sepsis dynamics.

To further interpret the results, we visualize the temporally evolving causal networks extracted from the kernel tensor learned by TULIK-VI in Figure 11, which indicates the inferred Granger causal relationships between medical indices. Node radii are proportional to the estimated baseline intensities $\mu(u)$; arrows represent excitatory effects, with arrow widths indicating the magnitude of influence. We present the five strongest edges at each time snapshot of the network.

The learned network structure aligns with medical knowledge. For example, the node “DCO” (Diminished Cardiac Output) consistently exhibits a strong excitatory influence on sepsis onset, an observation well-established in sepsis research [36]. Additionally, as time progresses, more medical indices show a strong influence on sepsis onset, reflecting the development of multiple organ dysfunction syndrome in severe cases. Figure 12 shows that the effects of biological processes are nonlinear, suggesting that medical indices cannot deteriorate indefinitely, nor can their influence on sepsis onset grow without bound.

8.2 Burglary crime data

Dataset. To validate our method on another dataset, we consider a proprietary dataset provided by the Atlanta Police Department (APD), including over 213,000 burglary events recorded from the beginning of 2013 to the end of 2019, with timestamps and geographic coordinates (longitude and latitude). We focus on the downtown area of Atlanta, defined by the longitude range $[-84.400, -84.375]$ and latitude range $[33.745, 33.770]$. Figure 13 displays the spatial distribution of burglary events in this area. Following the setup in [15], we uniformly divide the downtown area into 16 sub-regions, resulting in $V = 16$ nodes for the point process model. We treat each 24-hour period, from 12:00 AM to 11:59 PM, as one trajectory. The time horizon is defined as $(-\tau_{\max}, T] = (-8, 16]$, incorporating a one-hour uncertainty. The time grid includes $N = 16$ and $N' = 8$ intervals, each representing one hour. The processed dataset consists of 2,548 daily trajectories. We randomly

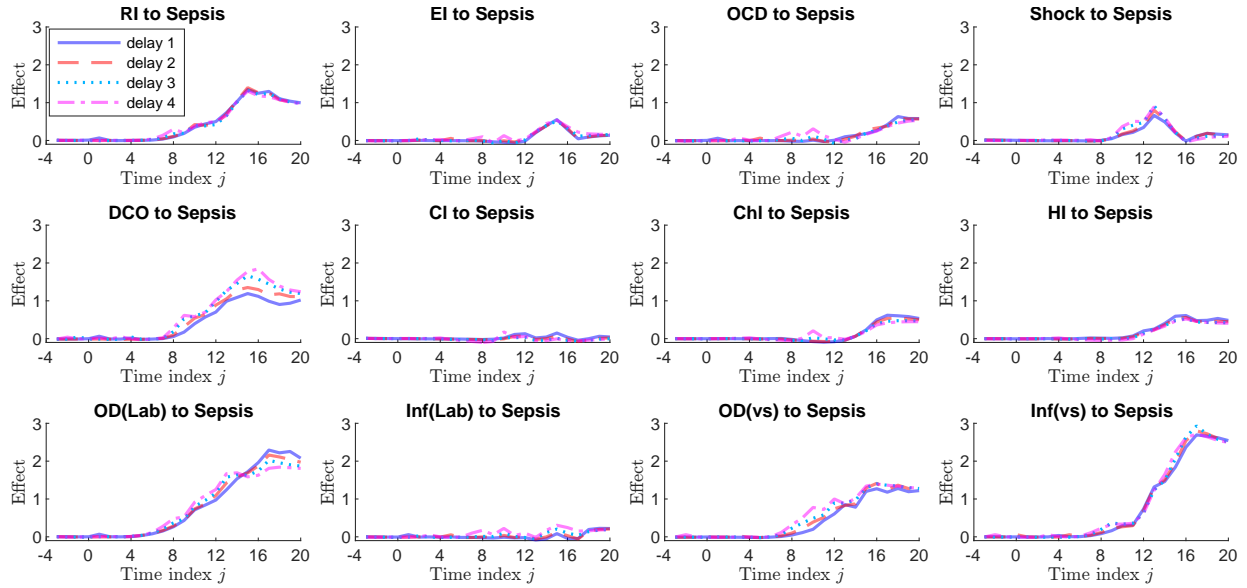


Figure 12: The effects from all medical indices to the sepsis onset over time across different delays.

select 2,250 for training and use the remaining 298 for testing.

Method. We compared TULIK-VI with GLM-L, GLM-S, and HP-E. Details of the hyperparameter tuning procedure are provided in Appendix D.5.2.

Results. Table 6 presents the prediction performance of all methods. We report TPR, TNR, and BA on the testing data. For the burglary crime data, TPR and TNR are computed by averaging across all nodes for $t \in (0, 16]$, treating event occurrences as positives and non-events as negatives. TULIK-VI achieves noticeably higher prediction accuracy compared to the baseline methods.

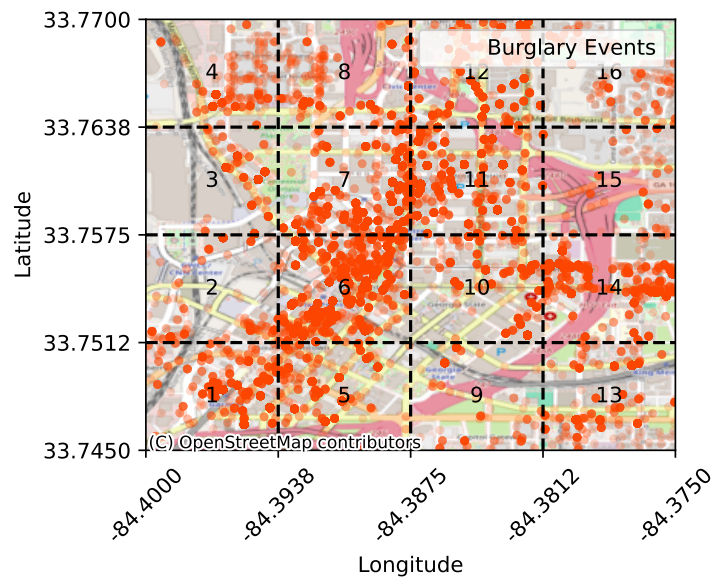


Figure 13: The distribution of the burglary crime events from 2013 to 2019 in the downtown Atlanta area.

Table 6: Crime data modeling in downtown Atlanta: TPR, TNR, and BAs from TULIK-VI. The time horizon is 1 day with an uncertainty of 1 hour. The standard deviations of TPR, TNR, and BA over 10 training replicas are in parentheses. The largest metrics are bolded.

	TULIK-VI	TULIK-VI (Stationary)	GLM-L	GLM-S	HP
TPR	0.6705 (0.0008)	0.6686 (0.0009)	0.6186 (0.0004)	0.6594 (0.0002)	0.4533 (0.0031)
TNR	0.6710 (0.0010)	0.6683 (0.0008)	0.6187 (0.0004)	0.6532 (0.0000)	0.4733 (0.0098)
BA	0.6707 (0.0002)	0.6684 (0.0004)	0.6187 (0.0003)	0.6563 (0.0001)	0.4633 (0.0036)

Again, we observe that TULIK, allowing for non-stationary modeling, outperforms its stationary counterpart. However, in this example, the performance gain is less pronounced than in the sepsis prediction case, suggesting that the burglary data may exhibit less non-stationarity. Nevertheless, TULIK still outperforms the alternative methods—GLM-L, GLM-S, and HP-E, the latter of which employs a parametric triggering kernel, highlighting the value of incorporating time uncertainty and flexible triggering structures.

9 Discussion

The work can be extended in several directions. First, although we focused on the unit-time uncertainty case in our algorithm development, our method can be extended to handle the arbitrary event uncertainty case in Section 3.2, applicable to both the time-only and on-network scenarios. Second, it would be useful to allow the baseline intensity μ to vary with time t , which can be handled within our discrete-time framework by introducing additional learnable parameters. Meanwhile, it would be interesting to relax the requirement that each uncertainty window contains exactly one event (Assumption 1), which would yield a Poisson process rather than a Bernoulli process and necessitate the development of a new time-uncertainty model. Finally, one can apply the approach to real-world data applications, and practical challenges may call for further development of computational techniques, e.g., the use of a barrier to enforce positive intensity and the tuning of optimization hyperparameters.

Acknowledgments

The work was partially supported by NSF DMS-2134037. YX was also partially supported by NSF DMS-2220495. XC was also partially supported by NSF DMS-2237842 and Simons Foundation (grant ID: 814643).

References

- [1] ABIM. American board of internal medicine: Laboratory reference ranges.
- [2] Emmanuel Bacry, Khalil Dayri, and Jean-François Muzy. Non-parametric kernel estimation for symmetric Hawkes processes. Application to high frequency financial data. *The European Physical Journal B*, 85(5):1–12, 2012.

- [3] Emmanuel Bacry, Sylvain Delattre, Marc Hoffmann, and Jean-François Muzy. Some limit theorems for Hawkes processes and application to financial statistics. *Stochastic Processes and their Applications*, 123(7):2475–2499, 2013.
- [4] Daryl J. Daley and David Vere-Jones. *An Introduction to the Theory of Point Processes. Volume I: Elementary Theory and Methods*. Springer, 2003.
- [5] Michele Dallachiesa, Besmira Nushi, Katsiaryna Mirylenka, and Themis Palpanas. Uncertain time-series similarity: Return to the basics. *Proceedings of the VLDB Endowment*, 5(11):1662–1673, 2012.
- [6] Zheng Dong, Xiuyuan Cheng, and Yao Xie. Spatio-temporal point processes with deep non-stationary kernels. In *Proceedings of the Eleventh International Conference on Learning Representations*, 2022.
- [7] Manisha Dubey, Ragja Palakkadavath, and PK Srijith. Bayesian neural Hawkes process for event uncertainty prediction. *International Journal of Data Science and Analytics*, pages 1–15, 2023.
- [8] Mehrdad Farajtabar, Nan Du, Manuel Gomez Rodriguez, Isabel Valera, Hongyuan Zha, and Le Song. Shaping social activity by incentivizing users. In *Advances in Neural Information Processing Systems*, volume 27, 2014.
- [9] Eric C Hall and Rebecca M Willett. Tracking dynamic point processes on networks. *IEEE Transactions on Information Theory*, 62(7):4327–4346, 2016.
- [10] Niels Richard Hansen, Patricia Reynaud-Bouret, and Vincent Rivoirard. Lasso and probabilistic inequalities for multivariate point processes. *Bernoulli*, 21(1):83–143, 2015.
- [11] Alan G Hawkes. Point spectra of some mutually exciting point processes. *Journal of the Royal Statistical Society: Series B (Methodological)*, 33(3):438–443, 1971.
- [12] Alan G Hawkes. Spectra of some self-exciting and mutually exciting point processes. *Biometrika*, 58(1):83–90, 1971.
- [13] Alan G Hawkes and David Oakes. A cluster process representation of a self-exciting process. *Journal of Applied Probability*, 11(3):493–503, 1974.
- [14] Niao He, Zaid Harchaoui, Yichen Wang, and Le Song. Point process estimation with mirror prox algorithms. *Applied Mathematics & Optimization*, 82(3):919–947, 2020.
- [15] Anatoli Juditsky, Arkadi Nemirovski, Liyan Xie, and Yao Xie. Convex parameter recovery for interacting marked processes. *IEEE Journal on Selected Areas in Information Theory*, 1(3):799–813, 2020.
- [16] Anatoli B Juditsky and AS Nemirovski. Signal recovery by stochastic optimization. *Automation and Remote Control*, 80(10):1878–1893, 2019.
- [17] Erik Lewis and George Mohler. A nonparametric EM algorithm for multiscale Hawkes processes. *Journal of Nonparametric Statistics*, 1(1):1–20, 2011.
- [18] André Luis S Maia, Francisco de AT de Carvalho, and Teresa B Ludermir. Forecasting models for interval-valued time series. *Neurocomputing*, 71(16-18):3344–3352, 2008.

- [19] David Marsan and Olivier Lengline. Extending earthquakes’ reach through cascading. *Science*, 319(5866):1076–1079, 2008.
- [20] Peter McCullagh. *Generalized linear models*. Routledge, 2019.
- [21] Hongyuan Mei and Jason M Eisner. The neural Hawkes process: A neurally self-modulating multivariate point process. In *Advances in Neural Information Processing Systems*, volume 30, 2017.
- [22] Yosihiko Ogata. Statistical models for earthquake occurrences and residual analysis for point processes. *Journal of the American Statistical Association*, 83(401):9–27, 1988.
- [23] Yosihiko Ogata. Estimating the hazard of rupture using uncertain occurrence times of paleoearthquakes. *Journal of Geophysical Research: Solid Earth*, 104(B8):17995–18014, 1999.
- [24] Yosihiko Ogata. Seismicity analysis through point-process modeling: A review. *Pure & Applied Geophysics*, 155(2-4):471, 1999.
- [25] Maya Okawa, Tomoharu Iwata, Yusuke Tanaka, Hiroyuki Toda, Takeshi Kurashima, and Hisashi Kashima. Dynamic Hawkes processes for discovering time-evolving communities’ states behind diffusion processes. In *Proceedings of the 27th ACM SIGKDD Conference on Knowledge Discovery & Data Mining*, pages 1276–1286, 2021.
- [26] Muhammad Osama, Dave Zachariah, and Peter Stoica. Prediction of spatial point processes: Regularized method with out-of-sample guarantees. In *Advances in Neural Information Processing Systems*, volume 32, 2019.
- [27] Alex Reinhart. A review of self-exciting spatio-temporal point processes and their applications. *Statistical Science*, 33(3):299–318, 2018.
- [28] Matthew A Reyna, Christopher S Josef, Russell Jeter, Supreeth P Shashikumar, M Brandon Westover, Shamim Nemati, Gari D Clifford, and Ashish Sharma. Early prediction of sepsis from clinical data: The PhysioNet/Computing in Cardiology Challenge 2019. *Critical Care Medicine*, 48(2):210–217, 2020.
- [29] Patricia Reynaud-Bouret and Sophie Schbath. Adaptive estimation for Hawkes processes; application to genome analysis. *The Annals of Statistics*, 38(5):2781–2822, 2010.
- [30] Marian-Andrei Rizoiu, Alexander Soen, Shidi Li, Pio Calderon, Leanne J Dong, Aditya Krishna Menon, and Lexing Xie. Interval-censored hawkes processes. *Journal of Machine Learning Research*, 23(338):1–84, 2022.
- [31] Philipp J Schneider and Thomas A Weber. Estimation of self-exciting point processes from time-censored data. *Physical Review E*, 108(1):015303, 2023.
- [32] Mervyn Singer, Clifford S Deutschman, Christopher Warren Seymour, Manu Shankar-Hari, Djillali Annane, Michael Bauer, Rinaldo Bellomo, Gordon R Bernard, Jean-Daniel Chiche, Craig M Coopersmith, et al. The third international consensus definitions for sepsis and septic shock (sepsis-3). *Jama*, 315(8):801–810, 2016.
- [33] Haoyun Wang, Liyan Xie, Alex Cuzzo, Simon Mak, and Yao Xie. Uncertainty quantification for inferring Hawkes networks. In *Advances in Neural Information Processing Systems*, volume 33, pages 7125–7134, 2020.

- [34] Song Wei and Yao Xie. Causal structural learning from time series: A convex optimization approach. In *2023 57th Asilomar Conference on Signals, Systems, and Computers*. IEEE, 2023.
- [35] Song Wei, Yao Xie, Christopher S Josef, and Rishikesan Kamaleswaran. Causal graph recovery for sepsis-associated derangements via interpretable Hawkes networks. In *International Conference on Machine Learning, Workshop on Interpretable Machine Learning in Healthcare (IMLH)*, 2021.
- [36] Song Wei, Yao Xie, Christopher S. Josef, and Rishikesan Kamaleswaran. Causal graph discovery from self and mutually exciting time series. *IEEE Journal on Selected Areas in Information Theory*, 4:747–761, 2023.
- [37] Song Wei, Yao Xie, Christopher S. Josef, and Rishikesan Kamaleswaran. Granger causal chain discovery for sepsis-associated derangements via continuous-time Hawkes processes. In *Proceedings of the 29th ACM SIGKDD Conference on Knowledge Discovery & Data Mining*, pages 2536–2546, 2023.
- [38] Junchi Yan, Chao Zhang, Hongyuan Zha, Min Gong, Changhua Sun, Jin Huang, Stephen Chu, and Xiaokang Yang. On machine learning towards predictive sales pipeline analytics. *Proceedings of the AAAI Conference on Artificial Intelligence*, 29(1), Feb. 2015.
- [39] Jian Yang, Peter J Weisberg, Thomas E Dilts, E Louise Loudermilk, Robert M Scheller, Alison Stanton, and Carl Skinner. Predicting wildfire occurrence distribution with spatial point process models and its uncertainty assessment: a case study in the Lake Tahoe Basin, USA. *International Journal of Wildland Fire*, 24(3):380–390, 2015.
- [40] Xiangfeng Yang and Baoding Liu. Uncertain time series analysis with imprecise observations. *Fuzzy Optimization and Decision Making*, 18(3):263–278, 2019.
- [41] Changyong Zhang. Modeling high frequency data using Hawkes processes with power-law kernels. *Procedia Computer Science*, 80:762–771, 2016.
- [42] Qingyuan Zhao, Murat A Erdogdu, Hera Y He, Anand Rajaraman, and Jure Leskovec. Seismic: A self-exciting point process model for predicting tweet popularity. In *Proceedings of the 21th ACM SIGKDD International Conference on Knowledge Discovery & Data Mining*, pages 1513–1522, 2015.
- [43] Ke Zhou, Hongyuan Zha, and Le Song. Learning social infectivity in sparse low-rank networks using multi-dimensional Hawkes processes. In *Proceedings of the Sixteenth International Conference on Artificial Intelligence and Statistics*, volume 31, pages 641–649, 2013.
- [44] Ke Zhou, Hongyuan Zha, and Le Song. Learning triggering kernels for multi-dimensional Hawkes processes. In *Proceedings of the 30th International Conference on Machine Learning*, volume 28, pages 1301–1309, 2013.
- [45] Jiancang Zhuang. Next-day earthquake forecasts for the Japan region generated by the ETAS model. *Earth, Planets and Space*, 63(3):207–216, 2011.
- [46] Jiancang Zhuang, Yosihiko Ogata, and David Vere-Jones. Stochastic declustering of space-time earthquake occurrences. *Journal of the American Statistical Association*, 97(458):369–380, 2002.

A Proofs in Section 3

Proof of Lemma 3.1. By Assumption (A1), we know that $\Delta_k^r > \Delta_k^l \geq \Delta_{k-1}^r$, and then we have

$$\begin{aligned} \Pr[\Delta_k | \tilde{\mathcal{F}}_{k-1}] &= S_k(\Delta_k^l) - S_k(\Delta_k^r) \\ &= \exp \left\{ - \int_{\Delta_{k-1}^r}^{\Delta_k^l} h_k(s) ds \right\} - \exp \left\{ - \int_{\Delta_{k-1}^r}^{\Delta_k^r} h_k(s) ds \right\} \\ &= \exp \left\{ - \int_{\Delta_{k-1}^r}^{\Delta_k^r} h_k(s) ds \right\} \left(\exp \left\{ \int_{\Delta_k^l}^{\Delta_k^r} h_k(s) ds \right\} - 1 \right). \end{aligned} \quad (\text{A.1})$$

This leads to the expression of the likelihood \mathcal{L} as follows, denoting $\Delta_0^r = 0$,

$$\mathcal{L} = \Pr[t_1 \in \Delta_1, \dots, t_n \in \Delta_n, t_{n+1} > T] \quad (\text{A.2})$$

$$\begin{aligned} &= \Pr[\Delta_1] \Pr[\Delta_2 | \tilde{\mathcal{F}}_1] \cdots \Pr[\Delta_n | \tilde{\mathcal{F}}_{n-1}] S_{n+1}(T) \\ &= \left(\prod_{k=1}^n \exp \left\{ - \int_{\Delta_{k-1}^r}^{\Delta_k^r} h_k(s) ds \right\} \left(\exp \left\{ \int_{\Delta_k^l}^{\Delta_k^r} h_k(s) ds \right\} - 1 \right) \right) \exp \left\{ - \int_{\Delta_n^r}^T h_{n+1}(s) ds \right\}. \end{aligned} \quad (\text{A.3})$$

Recall the definition of $\lambda(t)$ as in (16), then (A.3) can be written by integrals of $\lambda(t)$, which leads to the expression of \mathcal{L} as

$$\begin{aligned} \mathcal{L} &= \left(\prod_{k=1}^n \exp \left\{ - \int_{\Delta_{k-1}^r}^{\Delta_k^r} \lambda(u) du \right\} \left(\exp \left\{ \int_{\Delta_k^l}^{\Delta_k^r} \lambda(u) du \right\} - 1 \right) \right) \exp \left\{ - \int_{\Delta_n^r}^T \lambda(u) du \right\} \\ &= \left(\prod_{k=1}^n \left(\exp \left\{ \int_{\Delta_k^l}^{\Delta_k^r} \lambda(u) du \right\} - 1 \right) \right) \exp \left\{ - \int_0^T \lambda(u) du \right\}, \end{aligned}$$

Taking the log proves (17). □

Proof of Lemma 3.2. By (18) and under Assumption (A2), we have

$$\lambda(t) = \mu + \sum_{k, t_k^r < j} \frac{1}{h(t_k^r - t_k^l + 1)} \sum_{i=t_k^l}^{t_k^r} \int_{I_i} k(t', t) dt', \quad \forall t \in I_j.$$

By the definition of Λ_j in (21),

$$\Lambda_j = \mu + \sum_{k, t_k^r < j} \frac{1}{(t_k^r - t_k^l + 1)} \sum_{i=t_k^l}^{t_k^r} \frac{1}{h^2} \int_{I_i} \int_{I_j} k(t', t) dt' dt.$$

The expression (24) then follows by the definition of $K_{i,j}$ in (23). □

Proof of Lemma 3.3. Under (A3), the definition of Λ_t in (26) shows that $\Lambda_t \in \sigma\{y_i, i \leq t-1\}$. The expression of log-likelihood as in (26) gives that

$$\Pr[y_1, \dots, y_N] = e^\ell = \prod_{j=1}^N \left((1 - y_j) e^{-h\Lambda_j} + y_j (1 - e^{-h\Lambda_j}) \right).$$

This gives that, for any $t \in [N]$,

$$\Pr[y_1, \dots, y_t] = \prod_{j=1, y_j=1}^t (1 - e^{-h\Lambda_j}) \prod_{j=1, y_j=0}^t e^{-h\Lambda_j}.$$

Thus, by definition, $\Pr[y_t = 1 | y_i, i \leq t-1] = 1 - e^{-h\Lambda_t}$. \square

B Proofs in Section 4

B.1 Proofs in Section 4.3

Proof of Lemma 4.2. Consider when $t = -N' + 1$, since there is no history, $\Lambda_{-N'+1}^* = \mu$, and then (43) implies that $b \leq \mu \leq B$.

The claim that any realization of the binary sequence $\{y_t, -N' < t \leq N\}$ happens w.p. > 0 is equivalent to that any realization of the binary sequence $\{y_j, -N' + 1 \leq j \leq t\}$, for any $-N' < t \leq N$, happens w.p. > 0 . We prove this claim by induction. First, for $t = -N' + 1$, $\Pr[y_{-N'+1} = 0] = e^{-h\mu} \in (e^{-hB}, e^{-hb})$. Thus both $\Pr[y_{-N'+1} = 0]$ and $\Pr[y_{-N'+1} = 1] > 0$. Suppose the claim holds for $t-1$,

$$\begin{aligned} \Pr[(y_{-N'+1}, \dots, y_t)] &= \Pr[(y_{-N'+1}, \dots, y_{t-1})] \Pr[y_t | y_i, i \leq t-1] \\ &= \begin{cases} \Pr[(y_{-N'+1}, \dots, y_{t-1})] e^{-h\Lambda_t^*}, & y_t = 0 \\ \Pr[(y_{-N'+1}, \dots, y_{t-1})] (1 - e^{-h\Lambda_t^*}), & y_t = 1, \end{cases} \end{aligned}$$

where the second inequality is by Lemma 3.3. By induction hypothesis, $\Pr[(y_{-N'+1}, \dots, y_{t-1})] > 0$, then (43) holds a.s. means that Λ_t^* as a function evaluated at the outcome $(y_{-N'+1}, \dots, y_{t-1})$ needs to satisfy that $b \leq \Lambda_t^* \leq B$. This means that both $e^{-h\Lambda_t^*}$ and $1 - e^{-h\Lambda_t^*} > 0$. As a result, $\Pr[(y_{-N'+1}, \dots, y_t)] > 0$ in both cases of $y_t = 0$ or 1. This proves the claim for t based on the induction hypothesis on $t-1$. We thus have proved that the claim holds for any t .

Finally, because the conditional intensity Λ_t^* is a random variable determined by the outcome $(y_{-N'+1}, \dots, y_{t-1})$, any any realization of this binary sequence up to time $t-1$ happens w.p. > 0 , then $b \leq \Lambda_t^* \leq B$ a.s. means that for any realization of $(y_{-N'+1}, \dots, y_{t-1})$ this inequality holds. \square

Proof of Lemma 4.3. For any $v \in \mathbb{R}^{NN'}$, we also write v in the pattern of matrix K indexed by $v_{i,t}$, $-N' < i \leq N$, $1 \leq t \leq N$, cf. (31), then

$$\left\langle v, \left[\mathbb{E} \sum_{t=1}^N \eta_t \otimes \eta_t \right] v \right\rangle = \mathbb{E} \sum_{t=1}^N \langle \eta_t, v \rangle^2 = \mathbb{E} \sum_{t=1}^N \left(\sum_{i=-N'}^{t-1} y_i v_{i,t} \right)^2, \quad (\text{A.4})$$

where the second equality is by (33). For each t , we lower bound $\mathbb{E} \left(\sum_{i=-N'}^{t-1} y_i v_{i,t} \right)^2$ by enumerating over the realizations of $(y_{t-N'}, \dots, y_{t-1})$, a binary sequence of length N' , that equals $(0, \dots, 1, \dots, 0)$, namely only $y_i = 1$ for some i and the other y_j 's are all zero. By the derivation in the proof of Lemma 3.3, we know that

$$\Pr[(y_{t-N'}, \dots, y_{t-1}) = (0, \dots, \underset{i-th}{1}, \dots, 0) | y_i, i < t - N'] = (1 - e^{-h\Lambda_i^*}) \prod_{j=t-N', j \neq i}^{t-1} e^{-h\Lambda_j^*},$$

and then, applying Lemma 4.2, we have

$$\Pr[(y_{t-N'}, \dots, y_{t-1}) = (0, \dots, \underset{i-th}{1}, \dots, 0)] \geq e^{-hB(N'-1)}(1 - e^{-hb}) = \rho. \quad (\text{A.5})$$

As a result, for each t ,

$$\begin{aligned} \mathbb{E} \left(\sum_{i=t-N'}^{t-1} y_i v_{i,t} \right)^2 &\geq \sum_{i=t-N'}^{t-1} v_{i,t}^2 \Pr[(y_{t-N'}, \dots, y_{t-1}) = (0, \dots, \underset{i-th}{1}, \dots, 0)] \\ &\geq \rho \sum_{i=t-N'}^{t-1} v_{i,t}^2, \end{aligned}$$

and then

$$\mathbb{E} \sum_{t=1}^N \left(\sum_{i=t-N'}^{t-1} y_i v_{i,t} \right)^2 \geq \rho \sum_{t=1}^N \sum_{i=t-N'}^{t-1} v_{i,t}^2 = \rho \|v\|_2^2.$$

This proves the lemma by putting back to (A.4). \square

Proof of Lemma 4.4. By definition of $G(z)$ in (41), for any $z, \tilde{z} \in \Theta_K$,

$$\begin{aligned} \langle G(z) - G(\tilde{z}), z - \tilde{z} \rangle &= \mathbb{E} \sum_{t=1}^N (\phi(h\Lambda_t(z)) - \phi(h\Lambda_t(\tilde{z}))) \langle \eta_t, z - \tilde{z} \rangle \\ &= \mathbb{E} \sum_{t=1}^N (\phi(h\Lambda_t(z)) - \phi(h\Lambda_t(\tilde{z}))) (\Lambda_t(z) - \Lambda_t(\tilde{z})), \end{aligned} \quad (\text{A.6})$$

where in the second equality we used that $\Lambda_t(z) = \mu + \langle \eta_t, z \rangle$. Observe an elementary fact about the function $\phi(x) = 1 - e^{-x}$: for any $\beta > 0$,

$$(\phi(x) - \phi(x'))(x - x') \geq e^{-\beta}(x - x')^2, \quad \forall x, x' \in (0, \beta). \quad (\text{A.7})$$

The claim can be verified by the Mean Value Theorem. Using this fact and that $\Lambda_t(z), \Lambda_t(\tilde{z}) \in [b, B]$ a.s. under Assumption 4(ii), (A.6) continues as

$$\langle G(z) - G(\tilde{z}), z - \tilde{z} \rangle \geq \mathbb{E} \sum_{t=1}^N e^{-hB} h \langle \eta_t, z - \tilde{z} \rangle^2 = e^{-hB} h \left\langle z - \tilde{z}, \left[\mathbb{E} \sum_{t=1}^N \eta_t \otimes \eta_t \right] (z - \tilde{z}) \right\rangle.$$

By Lemma 4.3 which holds under Assumption 4(i), we have

$$\langle G(z) - G(\tilde{z}), z - \tilde{z} \rangle \geq e^{-hB} h \rho \|z - \tilde{z}\|^2.$$

It remains to show that $e^{-hB} h \rho \geq \kappa$ to finish the proof of the lemma. By definition,

$$e^{-hB} h \rho = h(1 - e^{-hb})e^{-hBN'} \geq h^2 b e^{-hb} e^{-hBN'} = \kappa,$$

by that $hN' = \tau_{\max}$, where in the inequality we used the fact that $xe^{-x} \leq 1 - e^{-x}$, $\forall x \geq 0$. \square

• Proof of Theorem 4.5

The proof of Theorem 4.5 uses the following technical lemma on the boundedness of the (per-trajectory) VI vector field.

Lemma B.1. *Under Assumption 4, let C be as defined in Theorem 4.5,*

(i) *Define $G_1(z) := \mathbb{E} \sum_{t=1}^N \phi(h\Lambda_t(z))\eta_t$, then $\forall z \in \Theta_K$, $\|G_1(z)\|_2 \leq C$.*

(ii) *$\forall z \in \Theta_K$, $\mathbb{E}\|\hat{G}^{(m)}(z)\|_2^2 = \mathbb{E}\|\sum_{t=1}^N (\phi(h\Lambda_t(z)) - y_t)\eta_t\|_2^2 \leq 4C^2$.*

Proof of Lemma B.1. We first prove (i), which provides useful intermediate estimates to prove (ii). The norm $\|\cdot\|$ always denotes 2-norm.

Proof of (i): $\|G_1(z)\|^2 = \|\mathbb{E} \sum_{t=1}^N \phi(h\Lambda_t(z))\eta_t\|^2 \leq \mathbb{E}\|\sum_{t=1}^N \phi(h\Lambda_t(z))\eta_t\|^2$ by Jensen's inequality. By definition of η_t as a vector in $\mathbb{R}^{NN'}$, we know that $\langle \eta_t, \eta_{t'} \rangle = 0$ when $t \neq t'$. Meanwhile, $\|\eta_t\|^2 = \sum_{i=t-N'}^{t-1} y_i$. Thus,

$$\mathbb{E}\|\sum_{t=1}^N \phi(h\Lambda_t(z))\eta_t\|^2 = \mathbb{E}\sum_{t=1}^N \phi(h\Lambda_t(z))^2 \sum_{i=t-N'}^{t-1} y_i \leq ((hB) \wedge 1)^2 \mathbb{E}\sum_{t=1}^N \sum_{i=t-N'}^{t-1} y_i,$$

where the 2nd inequality is by that, under Assumption 4(ii),

$$0 \leq \phi(h\Lambda_t(z)) = 1 - e^{-h\Lambda_t(z)} \leq 1 - e^{-hB} \leq (hB) \wedge 1 \quad a.s.,$$

using the elementary relation that $1 - e^{-x} \leq x$, $\forall x \geq 0$. We claim that

$$\mathbb{E}\sum_{t=1}^N \sum_{i=t-N'}^{t-1} y_i \leq NN'((hB) \wedge 1). \quad (\text{A.8})$$

If true, then putting together, we have

$$\begin{aligned} \|G_1(z)\|^2 &\leq \mathbb{E}\|\sum_{t=1}^N \phi(h\Lambda_t(z))\eta_t\|^2 \leq ((hB) \wedge 1)^2 \mathbb{E}\sum_{t=1}^N \sum_{i=t-N'}^{t-1} y_i \\ &\leq ((hB) \wedge 1)^3 NN' \leq ((hB) \wedge 1)^2 (N + N')^2, \end{aligned}$$

namely $\|G_1(z)\| \leq ((hB) \wedge 1)(N + N')$ which equals C since $hB(N + N') = B(T + \tau_{\max})$.

Proof of Claim (A.8): Observe that for any t , we always have

$$\mathbb{E}[y_t | y_i, i < t] = 1 - e^{-h\Lambda_t^*} \leq 1 - e^{-hB} \leq (hB) \wedge 1 \quad (\text{A.9})$$

by Lemma 3.3 and Lemma 4.2, and then

$$\mathbb{E}y_t = \mathbb{E}(\mathbb{E}[y_t | y_i, i < t]) \leq (hB) \wedge 1.$$

By linearity of expectation, we have

$$\mathbb{E}\sum_{t=1}^N \sum_{i=t-N'}^{t-1} y_i \leq \sum_{t=1}^N \sum_{i=t-N'}^{t-1} (hB) \wedge 1,$$

which proves the claim.

Proof of (ii): Again using that $\langle \eta_t, \eta_{t'} \rangle = 0$ when $t \neq t'$, and $\|\eta_t\|^2 = \sum_{i=t-N'}^{t-1} y_i$, we have

$$\begin{aligned}
\mathbb{E} \left\| \sum_{t=1}^N (\phi(h\Lambda_t(z)) - y_t) \eta_t \right\|^2 &= \mathbb{E} \sum_{t=1}^N (\phi(h\Lambda_t(z)) - y_t)^2 \sum_{i=t-N'}^{t-1} y_i \\
&\leq \mathbb{E} \sum_{t=1}^N 2 (\phi(h\Lambda_t(z))^2 + y_t) \sum_{i=t-N'}^{t-1} y_i \quad (\text{by that } y_t^2 = y_t) \\
&= 2 \left(\mathbb{E} \sum_{t=1}^N \phi(h\Lambda_t(z))^2 \sum_{i=t-N'}^{t-1} y_i + \mathbb{E} \sum_{t=1}^N y_t \sum_{i=t-N'}^{t-1} y_i \right). \tag{A.10}
\end{aligned}$$

In the proof of (i), we have already shown that $\mathbb{E} \sum_{t=1}^N \phi(h\Lambda_t(z))^2 \sum_{i=t-N'}^{t-1} y_i \leq C^2$. To handle the second term in the bracket, by (A.9) we have

$$\begin{aligned}
\mathbb{E} \sum_{t=1}^N y_t \sum_{i=t-N'}^{t-1} y_i &= \mathbb{E} \sum_{t=1}^N \mathbb{E}[y_t | y_i, i < t] \sum_{i=t-N'}^{t-1} y_i \\
&\leq ((hB) \wedge 1) \mathbb{E} \sum_{t=1}^N \sum_{i=t-N'}^{t-1} y_i \\
&\leq ((hB) \wedge 1)^2 NN', \quad (\text{by Claim (A.8)})
\end{aligned}$$

which again is upper bounded by C^2 as has been shown in the proof of (i). Putting together, we have that (A.10) is upper bounded by $4C^2$. \square

Proof of Theorem 4.5. Due to the projection operator in (39), we have that $z_k \in \Theta_K$ for all k . Let $\|\cdot\|$ always denote the 2-norm. By definition of the projection operator (40), the convexity of Θ_K and that $z^* \in \Theta_K$, we have

$$\|z_k - z^*\|^2 \leq \|z_{k-1} - \gamma_k \hat{G}^{(k)}(z_{k-1}) - z^*\|^2,$$

and by expanding the r.h.s. we have

$$\|z_k - z^*\|^2 \leq \|z_{k-1} - z^*\|^2 - 2\gamma_k \langle \hat{G}^{(k)}(z_{k-1}), z_{k-1} - z^* \rangle + \gamma_k^2 \|\hat{G}^{(k)}(z_{k-1})\|^2.$$

Taking expectation on both sides, and defining $d_k := \frac{1}{2} \mathbb{E} \|z_k - z^*\|^2$, we have

$$d_k \leq d_{k-1} - \gamma_k \mathbb{E} \langle \hat{G}^{(k)}(z_{k-1}), z_{k-1} - z^* \rangle + \frac{1}{2} \gamma_k^2 \mathbb{E} \|\hat{G}^{(k)}(z_{k-1})\|^2. \tag{A.11}$$

The third term on the r.h.s. is upper bounded by $2\gamma_k^2 C^2$ by Lemma B.1(ii).

To handle the second term on the r.h.s. of (A.11), first note that z_{k-1} is in the σ -algebra generated by up to $(k-1)$ -th trajectories, and then

$$\begin{aligned}
\mathbb{E} \langle \hat{G}^{(k)}(z_{k-1}), z_{k-1} - z^* \rangle &= \mathbb{E} \langle \mathbb{E}[\hat{G}^{(k)}(z_{k-1}) | y^{(m)}, m = 1, \dots, k-1], z_{k-1} - z^* \rangle \\
&= \mathbb{E} \langle G(z_{k-1}), z_{k-1} - z^* \rangle,
\end{aligned}$$

where we used that $\mathbb{E}[\hat{G}^{(k)}(z_{k-1}) | y^{(m)}, m = 1, \dots, k-1] = G(z_{k-1})$ because $y^{(k)}$ is independent from the previous $k-1$ trajectories. Next, recall (42), we have

$$\langle G(z_{k-1}), z_{k-1} - z^* \rangle = \langle G(z_{k-1}) - G(z^*), z_{k-1} - z^* \rangle \geq \kappa \|z_{k-1} - z^*\|^2,$$

where the last inequality is by Lemma 4.4 and that both z_{k-1} and z^* are in Θ_K . Taking expectations on both sides gives

$$\mathbb{E}\langle G(z_{k-1}), z_{k-1} - z^* \rangle \geq 2\kappa d_{k-1}.$$

Putting back to (A.11), we have

$$d_k \leq (1 - 2\kappa\gamma_k)d_{k-1} + 2\gamma_k^2 C^2, \quad (\text{A.12})$$

where, by our choice of γ_k , $\kappa\gamma_k = 1/(k+1) \leq 1/2$ for all $k \geq 1$, and thus, the factor $1 - 2\kappa\gamma_k$ is non-negative. We now claim that for all k ,

$$d_k \leq \frac{2C^2}{\kappa^2} \frac{1}{k+1}, \quad (\text{A.13})$$

which, if true, proves the theorem. The proof of (A.13) follows the argument to prove the same claim in the proof of [16, Proposition 2], and we include the details for completeness.

We prove (A.13) by induction. When $k = 0$, we have $d_0 \leq D^2/2$ where $D > 0$ is the diameter of the domain Θ_K . Suppose $D = \|z_+ - z_-\|$, where $z_+, z_- \in \Theta_K$. We then have

$$\begin{aligned} \kappa D^2 &= \kappa \|z_+ - z_-\|^2 \leq \langle G(z_+) - G(z_-), z_+ - z_- \rangle \quad (\text{by Lemma 4.4}) \\ &= \langle \mathbb{E} \sum_{t=1}^N (\phi(h\Lambda_t(z_+)) - \phi(h\Lambda_t(z_-))) \eta_t, z_+ - z_- \rangle \\ &= \langle G_1(z_+) - G_1(z_-), z_+ - z_- \rangle \quad (\text{by definition of } G_1 \text{ in Lemma B.1(i)}) \\ &\leq (\|G_1(z_+)\| + \|G_1(z_-)\|) \|z_+ - z_-\| \\ &\leq 2CD. \quad (\text{by Lemma B.1(i)}) \end{aligned}$$

This gives that $D \leq 2C/\kappa$, and then we have

$$d_0 \leq \frac{D^2}{2} \leq \frac{2C^2}{\kappa^2} =: S,$$

which proves (A.13) when $k = 0$.

Suppose the claim holds up to $k-1$; we prove it also holds for k . Because $k \geq 1$, we have $1 - 2\kappa\gamma_k \geq 0$, then, by (A.12), and that $d_{k-1} \leq S/k$ (the induction hypothesis),

$$\begin{aligned} d_k &\leq (1 - 2\kappa\gamma_k) \frac{S}{k} + 2\gamma_k^2 C^2 \\ &\leq \frac{S}{k} \left(1 - \frac{2}{k+1}\right) + \frac{S}{(k+1)^2} \quad (\text{by definitions of } \gamma_k \text{ and } S) \\ &= \frac{S}{k+1} \left(\frac{k-1}{k} + \frac{1}{k+1}\right) \leq \frac{S}{k+1}. \end{aligned}$$

This proves the claim (A.13) by induction. □

B.2 Proofs in Section 4.2

Proof of Proposition 4.1. Direct computation gives that

$$\partial_{zz}^2 \mathbb{E}(-L(z)) = \mathbb{E} \sum_{t=1}^N \frac{h^2}{\phi(h\Lambda_t(z))^2} e^{-h\Lambda_t(z)} y_t \eta_t \otimes \eta_t. \quad (\text{A.14})$$

For any $z \in \Theta_K$, by Assumption 4(ii), $b \leq \Lambda_t(z) \leq B$ a.s., and then $\frac{e^{-h\Lambda_t(z)}}{(1-e^{-h\Lambda_t(z)})^2} \geq \frac{e^{-hB}}{(1-e^{-hB})^2}$ a.s. This gives that

$$\partial_{zz}^2 \mathbb{E}(-L(z)) \succeq h^2 \frac{e^{-hB}}{(1-e^{-hB})^2} \mathbb{E} \sum_{t=1}^N y_t \eta_t \otimes \eta_t.$$

Meanwhile, because $\eta_t \in \sigma\{y_i, i < t\}$,

$$\begin{aligned} \mathbb{E} \sum_{t=1}^N y_t \eta_t \otimes \eta_t &= \mathbb{E} \sum_{t=1}^N \mathbb{E}[y_t | y_i, i < t] \eta_t \otimes \eta_t \\ &= \mathbb{E} \sum_{t=1}^N (1 - e^{-h\Lambda_t^*}) \eta_t \otimes \eta_t \quad (\text{by Lemma 3.3}) \\ &\succeq (1 - e^{-hb}) \mathbb{E} \sum_{t=1}^N \eta_t \otimes \eta_t, \quad (\text{by Lemma 4.2}) \\ &\succeq (1 - e^{-hb}) \rho I_{NN'}. \quad (\text{by Lemma 4.3}) \end{aligned}$$

This means that $\mathbb{E}(-L(z))$ is λ -strongly convex on Θ_K where $\lambda = h^2 \frac{e^{-hB}}{(1-e^{-hB})^2} (1 - e^{-hb}) \rho$. To prove the proposition, it suffices to show that $\lambda \geq \kappa'$. This can be verified by the definition of ρ in Lemma 4.3 and using that $xe^{-x} \leq 1 - e^{-x} \leq x$, $\forall x \geq 0$. \square

B.3 Proofs in Section 4.4

Proof of Lemma 4.6. We claim that under Assumption 4(i),

$$\mathbb{E} \sum_{t=1}^N \xi_t \otimes \xi_t \succeq \rho_s I_{N'}, \quad \rho_s := bT e^{-hb} e^{-hB(N'-1)}. \quad (\text{A.15})$$

If true, then using the same argument as in the proof of Lemma 4.4 one can show that for any $\psi, \tilde{\psi} \in \Theta_\psi$,

$$\begin{aligned} \langle G_s(\psi) - G_s(\tilde{\psi}), \psi - \tilde{\psi} \rangle &\geq e^{-hB} h \left\langle \psi - \tilde{\psi}, \left[\mathbb{E} \sum_{t=1}^N \xi_t \otimes \xi_t \right] (\psi - \tilde{\psi}) \right\rangle \\ &\geq e^{-hB} h \rho_s \|\psi - \tilde{\psi}\|_2^2, \end{aligned}$$

which proves that G_s is $(e^{-hB} h \rho_s)$ -monotone on Θ_ψ , and that is the same as declared in the lemma.

It remains to prove the claim (A.15) to prove the lemma. For any $v \in \mathbb{R}^{N'}$,

$$\left\langle v, \left[\mathbb{E} \sum_{t=1}^N \xi_t \otimes \xi_t \right] v \right\rangle = \mathbb{E} \sum_{t=1}^N \langle \xi_t, v \rangle^2 = \mathbb{E} \sum_{t=1}^N \left(\sum_{i=t-N'}^{t-1} y_i v_{t-i} \right)^2.$$

To lower bound $\mathbb{E} \left(\sum_{i=t-N'}^{t-1} y_i v_{t-i} \right)^2$ for each t , again we have (A.5) due to Lemma 4.2, and then

$$\mathbb{E} \left(\sum_{i=t-N'}^{t-1} y_i v_{t-i} \right)^2 \geq \rho \sum_{i=t-N'}^{t-1} v_{t-i}^2 = \rho \|v\|_2^2, \quad \rho = e^{-hB(N'-1)} (1 - e^{-hb}).$$

Thus, $\mathbb{E} \sum_{t=1}^N \left(\sum_{i=t-N'}^{t-1} y_i v_{t-i} \right)^2 \geq N\rho \|v\|_2^2$. This proves that $\mathbb{E} \sum_{t=1}^N \xi_t \otimes \xi_t \succeq \lambda I_{N'}$ where

$$\lambda = N\rho = Ne^{-hB(N'-1)}(1 - e^{-hb}) \geq Ne^{-hB(N'-1)}hbe^{-hb} = \rho_s,$$

where in the inequality we used $xe^{-x} \leq 1 - e^{-x}$, $\forall x \geq 0$. \square

C Proofs in Section 5

Proof of Lemma 5.1. Using the expression (54), we have that, denoting $\Delta_0^r = 0$,

$$\begin{aligned} \mathcal{L} &= \Pr[(\Delta_1, u_1)] \Pr[(\Delta_2, u_2)|\tilde{\mathcal{F}}_1] \cdots \Pr[(\Delta_n, u_n)|\tilde{\mathcal{F}}_{n-1}] S_{n+1}(T) \\ &= \prod_{k=1}^n \left(e^{-\int_{\Delta_{k-1}^r}^{\Delta_k^r} \bar{\lambda}(s) ds} \int_{\Delta_k^l}^{\Delta_k^r} \lambda(t, u) e^{\int_t^{\Delta_k^r} \bar{\lambda}(s) ds} dt \right) e^{-\int_{\Delta_n^r}^T \bar{\lambda}(s) ds} \\ &= e^{-\int_0^T \bar{\lambda}(s) ds} \prod_{k=1}^n \left(\int_{\Delta_k^l}^{\Delta_k^r} \lambda(t, u_k) e^{\int_t^{\Delta_k^r} \bar{\lambda}(s) ds} dt \right). \end{aligned}$$

This proves the expression (55). \square

Proof of Lemma 5.2. Under (A3), $\Delta_i = I_{j(i)}$ for some $j(i) \in [N]$, and then for $t \in I_j$, by (57),

$$\lambda[k](t, u) = \mu(u) + \sum_{i, j(i) < j} \frac{1}{h} \int_{I_{j(i)}} k(t', t; u_i, u) dt',$$

because $\Delta_i^r < t$ if and only if $j(i) < j$. By Assumption 5, for $t' \in I_{j(i)}$ and $t \in I_j$, $k(t', t; u_i, u) \equiv K_{j(i), j}(u_i, u)$. Thus,

$$\lambda[k](t, u) = \mu(u) + \sum_{i, j(i) < j} K_{j(i), j}(u_i, u), \quad \forall t \in I_j.$$

The r.h.s. is a constant independent of t , and this proves the lemma. \square

Proof of Lemma 5.3. Under (A3), we have (58) hold, namely

$$\ell = \sum_{k=1}^n \log \left(\int_{I_{j(k)}^l}^{I_{j(k)}^r} \lambda(t, u_k) e^{\int_t^{I_{j(k)}^r} \bar{\lambda}(s) ds} dt \right) - \int_0^T \bar{\lambda}(s) ds.$$

Applying Lemma 5.2, we have

$$\int_{I_{j(k)}^l}^{I_{j(k)}^r} \lambda(t, u_k) e^{\int_t^{I_{j(k)}^r} \bar{\lambda}(s) ds} dt = \Lambda_{j(k)}(u_k) \int_0^h e^{\bar{\Lambda}_{j(k)}(h-t)} dt = \frac{\Lambda_{j(k)}(u_k)}{\bar{\Lambda}_{j(k)}} (e^{h\bar{\Lambda}_{j(k)}} - 1),$$

and meanwhile,

$$\int_0^T \bar{\lambda}(s) ds = \sum_{j=1}^N h\bar{\Lambda}_j.$$

This proves the expression of ℓ as (61). \square

Proof of Lemma 5.4. The expression (66) implies that $\mathbf{\Lambda}_t$ is in $\sigma\{\mathbf{y}_i, i \leq t-1\}$. From the expression of the log-likelihood (67), one can verify that

$$\Pr[\bar{y}_t = 1 | \mathbf{y}_i, i \leq t-1] = 1 - e^{-h\bar{\Lambda}_t},$$

and for each $u \in \mathcal{V}$,

$$\Pr[y_t(u) = 1 | \mathbf{y}_i, i \leq t-1, \bar{y}_t = 1] = \frac{\Lambda_t(u)}{\bar{\Lambda}_t}.$$

As a result,

$$\Pr[y_t(u) = 1 | \mathbf{y}_i, i \leq t-1] = (1 - e^{-h\bar{\Lambda}_t}) \frac{\Lambda_t(u)}{\bar{\Lambda}_t} = (1 - e^{-h\mathbf{\Lambda}_t^T \mathbf{1}}) \frac{\Lambda_t(u)}{\mathbf{\Lambda}_t^T \mathbf{1}},$$

where in the second equality we used that $\bar{\Lambda}_t = \mathbf{\Lambda}_t^T \mathbf{1}$ by definition (60). Writing in vector form, this gives $\mathbb{E}[\mathbf{y}_t | \mathbf{y}_i, i \leq t-1] = \Phi(\mathbf{x})$ with $\mathbf{x} = h\mathbf{\Lambda}_t \in \mathbb{R}_+^V$. \square

D Additional experimental details

D.1 On the time-only data in Section 7.1

D.1.1 Choice of hyperparameters

In the experiment with $N = 32$ and $N' = 8$: The batch size $M_B = 400$, and the maximum number of epochs $k_{\max} = 300$. Learning rate: for TULIK-VI, the schedule is set as $\gamma_k = 0.4$ if $k \leq 100$ and $\gamma_k = 0.2$ if $100 < k \leq 300$; for TULIK-GD, the schedule is set as $\gamma_k = 0.2$ if $k \leq 100$ and $\gamma_k = 0.1$ if $100 < k \leq 300$. Regularization: We use the quadratic barrier in (76), the intensity lower bound $b = 0.01$, the barrier weight $\delta_b = 0.1$. We apply the smoothness penalty (77) with smoothness weight $\delta_s = 0.08$.

In the experiment with $N = 320$ and $N' = 80$: all the choices of optimization hyperparameters are the same as the experiment with $N = 32$ and $N' = 8$ except for $\delta_s = 0.004$. We apply low-rank truncation after the stochastic optimization loops. We select the singular value threshold $\tau_{\text{SVD}} \in \{0.2, 0.4, \dots, 1.2\}$ by minimizing the ℓ_1 probabilistic prediction errors on a validation set with 500 trajectories. This gives $\tau_{\text{SVD}} = 0.6$ and 0.8 for TULIK-VI and TULIK-GD respectively. The truncated kernel matrices have rank 3 for both cases and are plotted in Figure 6.

D.1.2 Training dynamics for the data with $N = 32$ and $N' = 8$

Figure A.1a shows the descending dynamics of training negative log-likelihood functions for both TULIK-VI and TULIK-GD. Meanwhile, Figure A.1b shows that the proposed scheme to learn μ also numerically converges to the truth $\mu = 0.2$ in both TULIK-VI and TULIK-GD.

D.1.3 Alternative baselines

Note that in the GLM model [15], one can allow GLM-L and GLM-S to have non-stationary coefficients. In GLM, the standard approach to infer parameters is to construct the likelihood function and recover the parameters as MLE [20]. In the work proposing GLM-S and GLM-I, GLMs are used as part of the model for the Bernoulli processes and they train models using VI approach, which is originally introduced in [16] to adapt to problems with weaker assumptions than the convexity of the likelihood function.

Algorithm 2: Stochastic batch-based training for network case

Input : Training trajectories $\{\mathbf{y}_t^{(m)}\}_{m=1}^M$, $\boldsymbol{\mu}_0$ as initial value of $\boldsymbol{\mu}$; Parameters: intensity lower bound b , barrier weight δ_b ; batch size M_B , maximum number of epochs k_{\max} , learning rate schedule $\{\gamma_k\}_k$; Optional: singular value threshold τ_{SVD} , smoothness weight δ_s

Output : Learned kernel θ_K and baseline $\boldsymbol{\mu}$

```
1 Initialize kernel  $\theta_K \leftarrow 0$  and baseline on graph  $\boldsymbol{\mu} \leftarrow \boldsymbol{\mu}_0$ 
2 for  $k = 1, \dots, k_{\max}$  do
3   while loop over the batches do
4      $\theta \leftarrow [\boldsymbol{\mu}, \theta_K]$ 
5     Load  $M_B$  many training trajectories to form batch  $Y_B = \{\mathbf{y}^{(m)}\}_m$ 
6     Compute intensities  $\boldsymbol{\Lambda}_t^{(m)}[\theta]$  in (72) at  $t = 1, \dots, N$  for each  $\mathbf{y}^{(m)}$  in  $Y_B$ , and let
        $b^{(m)} \leftarrow \min_{1 \leq t \leq N, u \in \mathcal{V}} \Lambda_t^{(m)}(u)$ 
7     Split  $Y_B = Y_{B,1} \cup Y_{B,2}$ , where  $\mathbf{y}^{(m)}$  in  $Y_{B,1}$  if  $b^{(m)} < b$ , and otherwise in  $Y_{B,2}$ 
8     if using VI update then
9        $g_B \leftarrow \frac{1}{M_B} \sum_{\mathbf{y}^{(m)} \in Y_{B,2}} \hat{G}^{(m)}[\theta]$ ,  $\hat{G}^{(m)}$  as in (73)
10    else if using GD update then
11       $g_B \leftarrow \frac{1}{M_B} \sum_{\mathbf{y}^{(m)} \in Y_{B,2}} \hat{F}^{(m)}[\theta]$ ,  $\hat{F}^{(m)}$  as in (74)
12    end
13    if  $Y_{B,1}$  not empty then
14       $g_B \leftarrow g_B + \delta_b \sum_{\mathbf{y}^{(m)} \in Y_{B,1}} \partial_{\theta_K} B^{(m)}(\theta)$ ,  $B^{(m)}$  as in (79)
15    end
16    Update  $\theta_K \leftarrow \theta_K - \gamma_k g_B$ 
17    For each  $u \in \mathcal{V}$ , solve  $\tilde{\mu}(u)$  as root of (78) on  $Y_B$  using bisection search
18    Update  $\mu(u) \leftarrow 0.9\mu(u) + 0.1\tilde{\mu}(u)$ ,  $\forall u \in \mathcal{V}$ 
19  end
20  (Optional) if do smoothness regularization of kernel then
21     $\theta_K \leftarrow \theta_K - \gamma_k \delta_s \partial_{\theta_K} \sum_{u', u \in \mathcal{V}} S([\Psi_{i,l}(u', u)]_{i,l})$ ,  $S$  as in (77)
22  end
23 end
24 (Optional) if do low-rank truncation of kernel then
25  Rearrange entries in  $\theta_K$  into  $\{[\Psi_{i,l}(u', u)]_{i,l}, u', u \in \mathcal{V}\}$  and concatenate matrices
     $\boldsymbol{\Psi} \leftarrow [\Psi(u', u)]_{u', u \in \mathcal{V}}$ ,  $\boldsymbol{\Psi}$  has size  $(N + N')V^2 \times N'$ 
26  For each  $(u', u)$ ,  $\boldsymbol{\Psi}'(u', u) \leftarrow \Psi_{(N'+1):N, 1:N'}(u', u)$ , and concatenate matrices
     $\boldsymbol{\Psi}' \leftarrow [\boldsymbol{\Psi}'(u', u)]_{u', u \in \mathcal{V}}$ ,  $\boldsymbol{\Psi}'$  has size  $(N - N' + 1)V^2 \times N'$ 
27   $r \leftarrow$  number of singular values of  $\boldsymbol{\Psi}'$  larger than  $\tau_{\text{SVD}}$ 
28   $V \leftarrow$  first  $r$  right singular vectors of  $\boldsymbol{\Psi}'$ 
29   $\boldsymbol{\Psi} \leftarrow \boldsymbol{\Psi} V V^\top$ , and rearrange  $\boldsymbol{\Psi}$  into  $\theta_K$ 
30 end
31 return  $\boldsymbol{\mu}, \theta_K$ 
```

For GLM-based baselines, the L^2 loss is formally defined as $L_{\text{GLM}}(\theta) = \frac{1}{M} \sum_{m=1}^M \ell_{\text{GLM}}^{(m)}(\theta)$, where

$$\ell_{\text{GLM}}^{(m)}(\theta) = \frac{1}{2} \sum_{t=1}^N (\phi_{\text{GLM}}(\Lambda_t^{(m)}(\theta)) - y_t^{(m)})^2,$$

and the VI field can be derived similarly as in Section 4.3. The link function $\phi_{\text{GLM}}(x)$ can be selected from the linear function $x\mathbb{I}_{[0,1]}(x)$, where $\mathbb{I}_{[0,1]}(x)$ is an indicator function on $[0, 1]$, or the sigmoid function $1/(1 + e^{-x})$, corresponding to GLM-L or GLM-S.

The HP-E method trains on the continuous-time data, which, in this experiment, are converted from data with uncertainty by assigning $t_i = jh$ for the i -th $y_j = 1$. For the learning of HP-E, since we are using the exponential time-invariant kernel defined in Section 2.1, we solve the gradient for μ , α , and β and optimize using SGD.

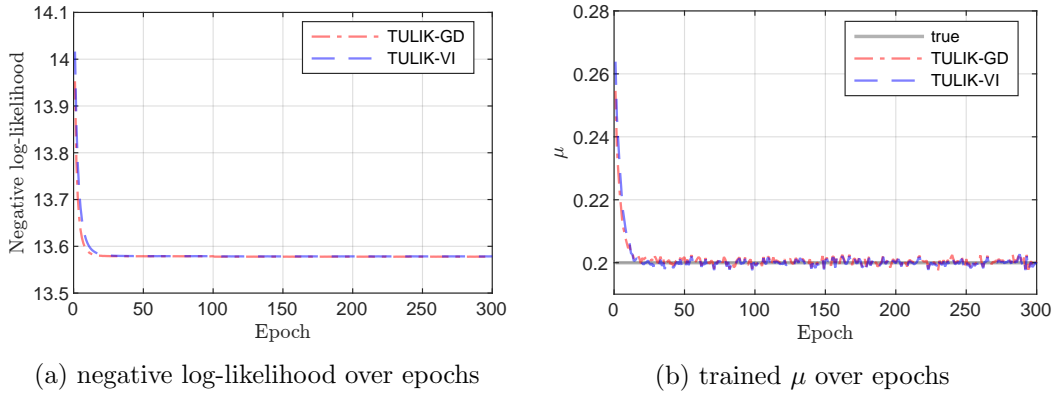


Figure A.1: Training dynamics on simulated time-only event data with kernel function defined in (80), $N' = 8$ and $N = 32$. (a) The training negative log likelihood over epochs of TULIK-GD and TULIK-VI. (b) The μ learned by TULIK-GD and TULIK-VI over epochs. The true value of μ is marked by the solid line at 0.2.

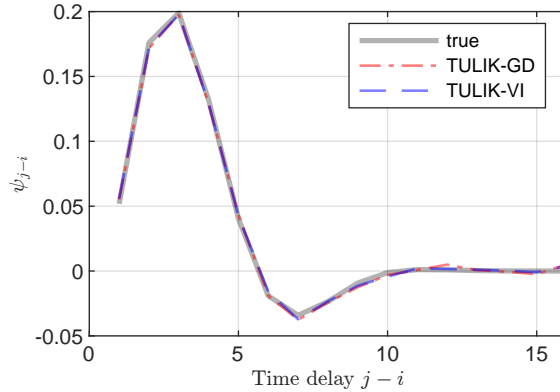


Figure A.2: True time-invariant kernel and recovered kernels on simulated time-only event data with $N' = 16$ and $N = 32$. True time-invariant kernel vector ψ is visualized as a solid curve. The kernels recovered by TULIK-VI and TULIK-GD are shown as a dashed curve and a dash-dotted curve, respectively.

Table A.1: Relative Errors (REs) of learned μ , kernel matrix, and probability predictions, on simulated time-only event data with the kernel vector ψ defined in Figure A.2 with $N' = 16$ and $N = 32$. The format are the same as in Table 1.

RE $\times 10^{-2}$	time-only event data with discrete time grids $N' = 16$ and $N = 32$								
	μ		kernel		prediction				
	TULIK-VI	TULIK-GD	TULIK-VI	TULIK-GD	TULIK-VI	TULIK-GD	GLM-L	GLM-S	HP-E
ℓ_1	0.70 (0.58)	0.60 (0.44)	10.73 (3.49)	9.99 (2.80)	2.00 (0.64)	1.89 (0.51)	2.28 (0.51)	5.26 (0.16)	47.19 (0.94)
ℓ_2	–	0.60 (0.44)	7.52 (2.51)	7.02 (2.06)	2.43 (0.77)	2.28 (0.62)	2.80 (0.63)	6.36 (0.31)	52.16 (0.94)
ℓ_∞	–	0.60 (0.44)	5.86 (2.36)	5.46 (2.11)	3.58 (1.10)	3.36 (0.90)	4.32 (1.12)	9.68 (1.07)	66.53 (0.95)

D.2 Simulated time-only event data with a time-invariant kernel

Dataset. We set discrete time grids as $N' = 16$ and $N = 32$ and define a true time-invariant kernel vector ψ visualized as the gray curve in Figure A.2. Given ψ and $\mu = 0.2$, we generate Bernoulli process data from (27). The training and testing data consist of 4800 and 500 trajectories, respectively.

Method. We compute the proposed model following Algorithm 1 and use the vector fields for the time-invariant kernel, which have been mentioned in Section 4.4. The choice of training hyperparameters is as follows: We set the batch size $M_B = 400$, and the maximum number of epochs $k_{\max} = 60$. Learning rate: for TULIK-VI, the learning rate schedule is set as $\gamma_k = 0.4$ if $k \leq 20$ and $\gamma_k = 0.2$ if $20 < k \leq 60$; for TULIK-GD, the learning rate schedule is set as $\gamma_k = 0.2$ if $k \leq 20$ and $\gamma_k = 0.1$ if $20 < k \leq 60$. Regularization: We use the quadratic barrier in (76), the intensity lower bound $b = 0.01$, the barrier weight $\delta_b = 0.1$. We apply the smoothness penalty (77) with smoothness weight $\delta_s = 0.004$.

We compare the proposed methods with the baselines including GLM-L, GLM-S, and HP-E, which can also be computed on the stationary example.

Results. In this time-invariant kernel example, the kernel ψ and the scalar μ are well recovered, as illustrated by Figure A.2 and the small REs in Table A.1. The probability predictions are also accurate, as shown in Figure A.3 and Table A.1. In comparison, TULIK methods outperform the other baselines, and in this case, the advantage over GLM-L is mild (within one standard deviation).

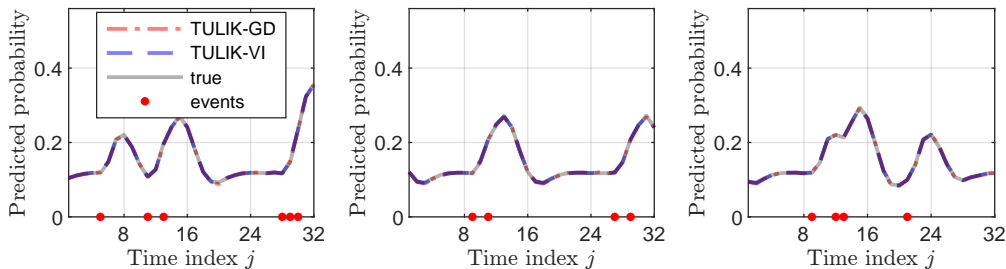


Figure A.3: The probability predictions on 3 randomly selected testing sequences. Data is the simulated time-only event data with time-invariant kernel vector ψ defined in Figure A.2 with $N' = 16$ and $N = 32$.

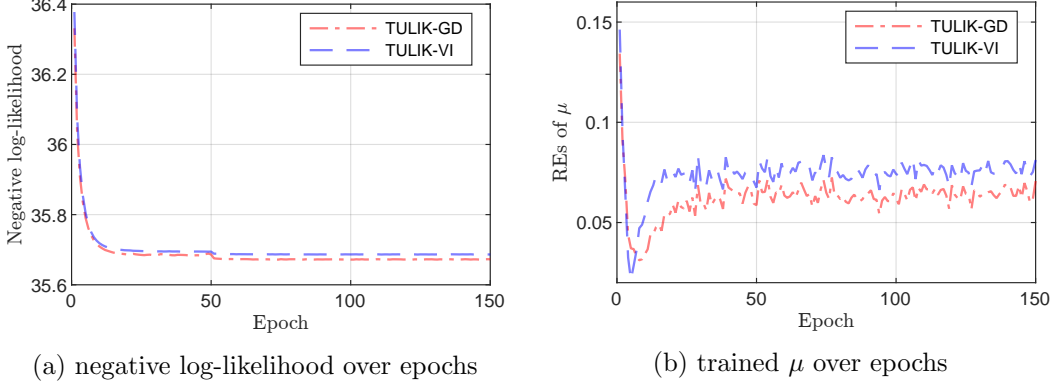


Figure A.4: For simulated on-network event data in Section 7.2, we train the model on 40000 trajectories using both TULIK-VI and TULIK-GD. The results from TULIK-VI and TULIK-GD are visualized as dashed curves and dash-dotted curves, respectively. (a) The dynamics of training negative log-likelihood over epochs. (c) The dynamics of REs of learned μ over epochs.

D.3 On the on-network data in Section 7.2

D.3.1 Choice of hyperparameters

We use the batch size $M_B = 800$ and the maximum number of epochs $k_{\max} = 150$. Learning rate: for TULIK-VI, the learning rate schedule is set as $\gamma_k = 0.4$ if $k \leq 50$ and $\gamma_k = 0.2$ if $50 < k \leq 150$; for TULIK-GD, the learning rate schedule is set as $\gamma_k = 0.2$ if $k \leq 50$ and $\gamma_k = 0.1$ if $50 < k \leq 150$. Regularization: we use the on-network quadratic barrier (79) with the intensity lower bound $b = 0.03$ and the barrier weight $\delta_b = 0.1$. We adopt the smoothness weight $\delta_s = 0.004$.

After the stochastic optimization loops, we apply low-rank truncation to the kernel matrix as in Algorithm 2. We select τ_{SVD} from $\{0.2, 0.4, \dots, 1.2\}$ by minimizing the ℓ_1 probabilistic prediction errors on a validation set with 500 trajectories, and obtain $\tau_{\text{SVD}} = 0.8$ and 1.0 for TULIK-VI and TULIK-GD respectively. The truncated matrices Ψ have rank-2 in both cases and are visualized in Figure 9.

D.3.2 Training dynamics

Figure A.4a shows the convergence of training log-likelihood functions for both TULIK-VI and TULIK-GD. Additionally, Figure A.4b validates the on-network approach to learning μ also numerically converges around 7% relative errors. Such relative errors correspond to absolute errors on each node around 0.01.

D.3.3 Alternative baselines

Note that for on-network event data, in both GLM-L and GLM-S, instead of the link functions, they use link vector field, which is the same link function as defined in time-only examples but implemented on each node, to compute the prediction probability. Their per-trajectory L^2 loss can be formally written as

$$\ell_{\text{GLM}}^{(m)}(z) = \frac{1}{2} \sum_{t=1}^N \|\Phi_{\text{GLM}}(\Lambda_t^{(m)}[z]) - \mathbf{y}_t^{(m)}\|_2^2,$$

where $\Phi_{\text{GLM}}(\mathbf{x}) = (\phi_{\text{GLM}}(x(u)))_{u \in \mathcal{V}}$. The VI monotone field used to update z can be derived similarly as in Section 5.4.

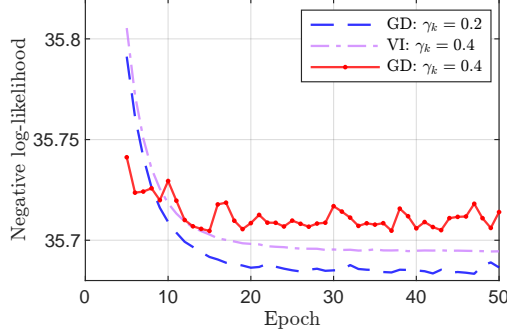


Figure A.5: Data is the on-network event data in Section 7.2. On the same training set, we increase the learning rate of GD to be 0.4 which is the same as VI, then the training negative log-likelihood oscillates and converges worse, showing instability in training.

For the learning of continuous-time multivariate HP-E, the kernel function becomes $k(t', t; u', u) = \alpha(u', u)\beta e^{-\beta(t-t')}$ and we perform SGD to learn $\boldsymbol{\mu}, (\alpha(u', u))_{u', u \in \mathcal{V}}$ and β .

D.3.4 Instability in GD training

Figure A.5 shows the dynamics of training negative log-likelihoods (from epoch 5 to epoch 50) for VI with a learning rate 0.4, and GD with a learning rate 0.2 and 0.4 respectively. It can be seen that, when the learning rate of GD is set to be the same as VI, the learning dynamic shows instability.

D.4 More on SADs data experiment in Section 8.1

We provide additional details for the SADs data and its results.

D.4.1 Data pre-processing

Table A.2 introduces the rules to group measurements into SADs and compute risk scores for SADs. The Bernoulli process $y_t(u)$ on the 13-node network is obtained from the risk scores on the first 12 nodes, and using spesis onset-or-not on the last node. Specifically, for the first 12 nodes, risk scores are assigned to indicate the severity of corresponding medical symptoms. Then for $u \in \{1, \dots, 12\}$, namely the nodes except for sepsis, $y_t(u) = 1$ means the risk score of node u increases at hour t .

D.4.2 Evaluation metrics

We evaluate the accuracy of sepsis onset prediction using the TPR, TNR, and BA. Since all patients in the processed data were eventually diagnosed as sepsis patients, the positive label cannot be defined simply based on sepsis onset. Instead, following the definition in [28], we consider a meaningful early prediction window $(t - 12, t]$ for a sepsis onset at time t . A patient is classified as *positive* if this prediction window intersects with the time horizon $(0, 20]$, ensuring that early prediction is feasible within the given time horizon. Specifically, patients with sepsis onset at $t < 32$ are labeled as positive, while those with onset at $t \geq 32$ are labeled as negative, as meaningful early prediction is not possible within the current time horizon for very late onsets. For a positive patient, a prediction is considered a true positive if the first predicted sepsis onset occurs within the early prediction window $(t - 12, t] \cap (0, 20]$; otherwise, it is classified as a false positive. For a negative patient, a prediction is considered a true negative if no sepsis onset is predicted within $(0, 20]$; otherwise, it is classified as a false negative.

Table A.2: SAD constructions based on raw observations thresholding and measurements grouping. For some measurement, if its raw observation exceed corresponding threshold, then its risk score will be added to the total risk score of corresponding SAD.

SAD name	Measurement name	Physionet name	Threshold	Risk score
Renal Injury	creatinine	Creatinine	>1.3	0.667
	potassium	Potassium	>5.0	0.067
	phosphorus	Phosphate	>4.5	0.067
	bicarb (hco3)	HCO3	>26	0.067
	blood urea nitrogen (bun)	BUN	>20	0.133
Electrolyte Imbalance	calcium	Calcium	>10.5	0.167
	chloride	Chloride	<98 or >106	0.667
	magnesium	Magnesium	<1.6	0.167
Oxygen Carrying Dysfunction	hematocrit	Hct	<37	0.500
	hemoglobin	Hgb	<12	0.500
Shock	base excess	BaseExcess	< -3	0.100
	lactic acid	Lactate	>2.0	0.150
	ph	pH	<7.32	0.750
Diminished Cardiac Output	sbp cuff	SBP	<120	0.250
	dbp cuff	DBP	<80	0.250
	map cuff	MAP	<65	0.500
Coagulopathy	partial prothrombin time (ptt)	PTT	>35	0.250
	fibrinogen	Fibrinogen	<233	0.250
	platelets	Platelets	<150,000	0.500
Cholestasis	bilirubin direct	Bilirubin direct	>0.3	0.100
	bilirubin total	Bilirubin total	>1.0	0.500
	alkaline phosphatase	Alkalinephos	>120	0.400
Hepatocellular Injury	aspartate aminotransferase (ast)	AST	>40	1.000
Oxygenation Dysfunction (lab)	saturation of oxygen (sao2)	SaO2	<92 %	0.500
	end tidal co2	EtCO2	<35 or >45	0.250
	partial pressure of carbon dioxide (paco2)	PaCO2	<35 or >45	0.250
Inflammation (lab)	glucose	Glucose	>125	0.200
	white blood cell count	WBC	<4,000 or >12,000	0.800
Oxygenation Dysfunction (vital)	unassisted resp rate	Resp	>20	0.167
	spo2	O2Sat	<92 %	0.333
	fiO2	FiO2	>21 %	0.500
Inflammation (vital)	temperature	Temp	<36 or >38	0.800
	pulse	HR	>90	0.200

D.4.3 Choice of hyperparameters

We initialize the kernel tensor by filling all zero. The initialization of on-network μ can refer to Section 6.2. To get reasonable results, we randomly leave one validation set containing 70 trajectories out of the training data. The remaining 1000 training trajectories will be used to update the kernel tensor and μ . We set the batch size $M_B = 107$, the maximum number of epochs $k_{\max} = 800$, and the learning rate schedule $\gamma_k = 0.4$ for all $k \leq 800$. We grid search the intensity lower bound $b \in \{0.002, 0.005, 0.01\}$, the barrier weight $\delta_b \in \{0.005, 0.01, 0.02\}$ in the quadratic loss, and the smoothness weight $\delta_s \in \{0.05, 0.1, 0.2\}$. Figure A.6 shows the validation curve for the search of optimal hyperparameters in the grid. We pick the hyperparameters that have the largest BA across different combinations. During the training, violations occur more frequently than the simulations but most of them will be corrected by the barrier penalty. For each set of hyperparameters, we compute the probability predictions on the validation set after training. Denote $\hat{p}_t(u)$ as the

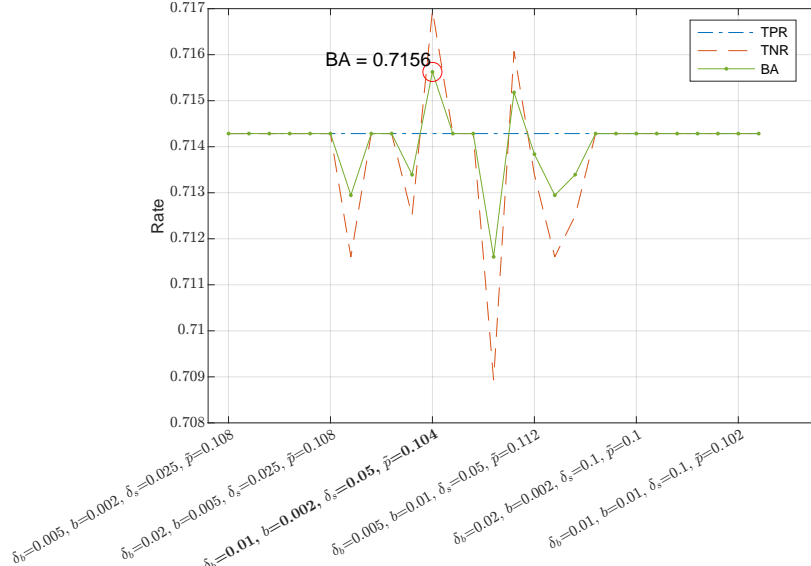


Figure A.6: After grid search in Section 8.1, the validation curve for SADs data learned by TULIK-VI. The curves with circle marker, with cross marker and with dot marker show TPR, TNR and BA over combinations of hyperparameters. The hyperparameters yielding largest BA on the validation set are bolded and the corresponding metrics on each curve are marked by red circles and texts.

prediction of $\mathbb{E}[y_t(u)|\mathbf{y}_i, i \leq t-1]$ in each method. We search for the probability threshold \tilde{p} between $[0, 1]$ to convert $\hat{p}_t(u) > \tilde{p}$ into ones and $\hat{p}_t(u) \leq \tilde{p}$ into zeros to minimize the absolute difference between TPR and TNR on the validation set. Then we select the hyperparameters yielding largest BA on the validation set for the eventual training on the whole training data.

D.5 On burglary crime data in Section 8.2

We introduce more details for the burglary data experiments.

D.5.1 Data pre-processing

As shown in Figure 13, the Atlanta downtown area is uniformly divided into 16 sub-regions, leading to 16 nodes in the point process model. The indices of the sub-region follow a latitude-major ascending order (bottom to top, left to right in Figure 13). The Bernoulli process $y_t(u)$ on the 16-node network is determined by burglary-or-not within the hour t at the sub-region u .

D.5.2 Choice of hyperparameters

We initialize the kernel tensor as a zero tensor. The initialization of on-network μ is introduced in Section 6.2. To obtain reasonable results, we randomly leave out a validation set with 250 trajectories from the training data. The remaining 2000 training trajectories are used to learn the kernel tensor and μ . We set the batch size to $M_B = 400$, the maximum number of epochs to $k_{\max} = 800$, and the learning rate schedule to $\gamma_k = 0.2$ for all $k \leq 800$. We perform a grid search over the intensity lower bound $b \in \{0.002, 0.005, 0.01\}$, the barrier weight $\delta_b \in \{0.005, 0.01, 0.02\}$ in the quadratic loss, and the smoothness weight $\delta_s \in \{0.05, 0.1, 0.2\}$. Figure A.7 presents the validation curve for the grid search of optimal hyperparameters. The hyperparameters that yield the highest BA across different combinations are selected. The search for the probability threshold

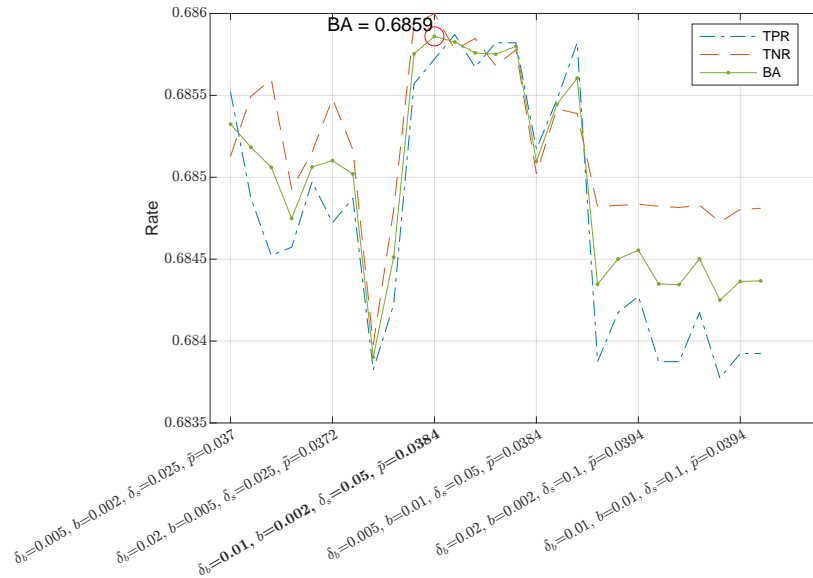


Figure A.7: Same plot as in Figure A.6. After grid search in Section 8.2, the validation curve for burglary crime data learned by TULIK-VI.

to convert the probability predictions to binary observations follows the same process as described in Section D.4.3.